Title: Rate limits and isotopologue fractionations for microbial methanogenesis examined with combined pathway protein cost and isotopologue flow network models

Shuhei Ono[1,*], Jeemin H. Rhim[1, †], Eric C. Ryberg[1]

[1] *Department of Earth, Atmospheric and Planetary Science, Massachusetts Institute of Technology, Cambridge, MA USA. sono@mit.edu, jrhim@alum.mit.edu, eryberg@mit.edu*

A revised manuscript (R1) prepared for submission to *Geochimica Cosmochimica Acta*

*corresponding author: sono@mit.edu

[†] present address: Department of Earth Sciences, Dartmouth College, Hanover, NH 03755, USA

Abstract

Microbial methanogenesis produces a range of isotope ($^{13}C/^{12}C$ and D/H) and isotopologue ($^{13}CH_3D$ and $^{12}CH_2D_2$) fractionations. Differential reversibility of enzymatic reactions qualitatively explains the isotope and isotopologue fractionations observed in both laboratory cultures and environmental samples. We applied pathway thermodynamics and isotopologue flow network models to quantitatively describe $^{13}C/^{12}C$, D/H, $^{13}CH_3D$, and $^{12}CH_2D_2$ fractionations during hydrogenotrophic methanogenesis. The model consists of the 10 enzymatic reactions of the methanogenesis pathway and tracks mass balance of isotopologues by taking into account the reaction symmetries of singly- and doubly-deuterated isotopologues. Based on the thermodynamics and enzyme kinetic data, the model estimates the reversibilities of 8 reactions from predicted *in vivo* concentrations of 17 metabolites and cofactors. The isotopologue flow network model calculates the isotopologue composition of product methane as well as all intermediates as a function of reversibilities and prescribed fractionation factors.

The model explains a number of observations for laboratory culture experiments, including the range of $^{13}C/^{12}C$ fractionation up to 80‰ between CH_4 and CO_2, with increasing magnitudes while decreasing pH_2. Relatively constant D/H fractionations of 300±40‰ between methane and water can be explained when methane is produced from three near-equilibrium H in methyl-coenzyme M with the addition of one kinetic D-depleted H during the last step of methanogenesis. Abundances of the doubly substituted isotopologues, $^{13}CH_3D$ and $^{12}CH_2D_2$, reflect kinetic and equilibrium end-members with additional complications due to non-linear mixing and/or combinatorial effect.

Our model can make predictions for isotopologue fractionations under slow rates of methanogenesis in energy-limiting deep sedimentary environments, where a large quantity of methane is produced. Near-equilibrium isotopologue ratios, often observed in marine sedimentary environments, are produced when pH_2 is less than 10 Pa. Our model results indicate that methanogenesis does not occur or only proceeds at extremely slow rates at this low pH_2 because low concentration of methyl-tetrahydromethanopterin limits the rate and

thermodynamic feasibility of methanogenesis. Accordingly, it is proposed that near-equilibrium methane isotopologue signals in deep marine sediments are produced by the catalytic reversibility of methyl-coenzyme M reductase, likely from anaerobic methanotrophic archaea performing either anaerobic methane oxidation or net methanogenesis. The pathway thermodynamics and isotopologue flow network model scheme presented herein can be applied and expanded to predict isotopologue fractionations for a range of metabolisms beyond methanogenesis.

1 Introduction

Methane is both an important energy source and a strong greenhouse gas. A group of microbes, called methanogens, is the major source of methane to the atmosphere as well as methane in deep sediments. Methanogens are strictly anaerobic Euryarchaeota specializing in the formation of methane from CO_2 and H_2 (hydrogenotrophic methanogenesis), formate, methanol, methylamines and/or acetate (Ferry, 1993; Thauer et al., 2008; Daniels, 1993).

Carbon ($^{13}C/^{12}C$) and hydrogen (D/H) isotope ratios have been widely used to trace the origin of methane in the environment (e.g., Whiticar, 1999). In addition to isotope ratios, the abundances of doubly substituted methane isotopologues ($^{13}CH_3D$ and $^{12}CH_2D_2$) have been proposed as proxies for the temperature of methane formation, although kinetic fractionations during microbial methane generation complicates their utility as geothermometers (e.g., Stolper et al., 2014; Stolper et al., 2015; Wang et al., 2015; Young et al., 2017). While these proxies are used as tools to fingerprint source(s) of methane, we do not understand, in particular, the origin of methane commonly observed in marine environments that often show intermolecular (H_2O versus CH_4) and intramolecular ($^{13}CH_3D$ and $^{12}CH_2D_2$) equilibria because laboratory methanogen cultures so far have exclusively produced methane with strong kinetic isotope and isotopologue signals (e.g., Valentine et al., 2004; Okumura et al., 2016; Stolper et al., 2015; Wang et al., 2015; Young et al., 2017).

Isotope and isotopologue compositions of methane in the environment can be generally grouped into kinetic (disequilibrium) and equilibrium populations (Wang et al.,2015; Okumura et al., 2016; Stolper et al., 2015; Gropp et al., 2021). Methane from surface freshwater environments (e.g., lakes, wetlands) and ruminants often exhibit strong kinetic signals in both $^{13}C/^{12}C$ and D/H ratios (against CO_2 and H_2O, respectively). They are characterized by relatively high $\delta^{13}C$ values and low D/H fractionation factors of 0.70±0.04 against water (Okumura et al.,2016; Waldron et al., 1999). In contrast, methane from marine sediments often yields $^{13}C/^{12}C$ and D/H ratios close to those expected under equilibrium against CO_2 and H_2O, respectively (with D/H fractionation factors of 0.81 ± 0.02 against water) (Whiticar, 1999; Okumura et al, 2016). There are two schools of interpretation for the origin of kinetic versus equilibrium signals. One relates different isotope signals to the rate of methanogenesis as slow methanogenesis in marine environments generate methane with near-equilibrium isotope signals and fast methanogenesis in shallow freshwater environments produces kinetic isotope signals (Meister et al., 2019; Okumura et al., 2016; Wang et al., 2015; Jautzy et al., 2021; Turner et al., 2021). The other associates the kinetic (D-depleted) signals with the predominance of acetoclastic methanogenesis in freshwater environments (e.g., Whiticar, 1999). The latter implies that the equilibrium methane in marine environments is produced by equilibration during anaerobic

oxidation of methane (e.g., Ash et al., 2019; Giunta et al., 2019; 2021; Warr et al., 2021). Therefore, one of the critical questions regarding the origin of kinetic vs. equilibrium isotope signals is if microbial methanogenesis can produce methane with (near-)equilibrium isotope and isotopologue signals.

The differential reversibility model (Valentine et al., 2004) was proposed to explain a range of carbon isotope fractionations during microbial methanogenesis. The model suggests that the magnitude of fractionation reflects the reversibilities of reactions in the pathway of methanogenesis and has been expanded to explain deuterium and isotopologue fractionations (e.g., Okumura et al., 2016; Stolper et al., 2015; Wang et al., 2015). The model qualitatively explains the isotope fractionations between equilibrium and kinetic end-members, as previous models used prescribed reversibilities (Stolper et al., 2015; Cao et al.,2019) or used an empirical function to describe them (Wang et al., 2015) (*see* Gropp et al., 2021 for a review of existing models).

We present a model that links pathway thermodynamic and isotopologue flow network models to quantitatively describe isotopologue fractionations as a function of energy availability by hydrogen concentrations. The model takes advantage of the available knowledge about energy conservation of methanogenesis (Thauer et al., 2008) and applies it to the pathway thermodynamics protein cost model by Flamholz et al. (2013) to derive reversibilities of reactions based on the flux-force relationship. We then apply kinetic isotope fractionation factors experimentally derived from *in vitro* methanogenesis (Scheller et al.,2013) and theoretically derived equilibrium fractionation factors (Gropp et al.,2021) to construct a pathway protein cost-isotope flux model that explicitly tracks singly- and doubly-substituted isotopologues for all intermediate metabolites. Our approach follows the Wing and Halevy (2014) model to predict sulfur isotope fractionations by sulfate reducers, but our model explicitly quantifies protein in addition to metabolite concentrations. We also show that the slow dissolution rate of H_2 gas often limits the rate of methanogenesis in laboratory cultures such that methanogens are exposed to much lower H_2 concentrations than expected from saturation against gaseous H_2. The model explains a number of observations for previous laboratory culture experiments, including the range of $^{13}C/^{12}C$ fractionation between CH_4 and CO_2 up to 80‰ (with increasing magnitudes at decreasing pH_2), commonly observed D/H fractionations of 300±40‰ that are relatively constant against pH_2, and the range of $^{13}CH_3D$ and $^{12}CH_2D_2$ abundances (e.g., Okumura et al., 2016; Penning et al., 2005; Gruen et al., 2018; Stolper et al., 2015; Young et al., 2017).

2 Method

2.1 The model of energy conservation for methanogens without cytochromes

The overall reaction for hydrogenotrophic methanogenesis can be written as:

$$CO_2 + 4H_2 \rightarrow CH_4 + 2H_2O \qquad (1)$$

The reaction yields Gibbs free energy of –131 kJ/mol CH_4 at standard conditions (i.e., CO_2, H_2 and CH_4 at 10^5 Pa at 25°C, Thauer et al., 2008). The free energy change of the overall methanogenesis reaction is shared among the multiple reactions in the pathway. In this work, we used the model of energy conservation for methanogens without cytochromes (Figure 1, Thauer et al., 2008). Methanogens without cytochromes represent those specialized in

hydrogenotrophic methanogenesis and are characterized by a higher affinity to H_2 and lower growth yields compared to methanogens with cytochromes. Methanogens with cytochromes are members of Methanosarcinales that are capable of using diverse substrates, including acetate and methanol (Thauer et al., 2008). In our model, the hydrogenotrophic methanogenesis pathway is represented in 10 reactions shown in Figure 1 and Table 1. Methanogens reduce CO_2 to CH_4 by a series of 7 reactions among which four reactions (reactions-1, 4, 5, and 7) are two electron transfer reactions that add H atoms to carbon, and reactions-6 and 7 are energy yielding reactions. The first step, reduction of CO_2 to formyl-methanofuran (formyl-MFR), requires reduced ferredoxin at ca. –500 mV SHE (potential against standard hydrogen electrode), which is lower than the redox potential of the H_2/H^+ pair (–413 mV SHE at 1 bar H_2 and pH=7). It has been shown that methanogens reduce ferredoxin via an electron bifurcation reaction in which the highly exergonic reduction of heterodisulfide (CoM-S-S-CoB) is coupled to the endergonic reduction of ferredoxin (reaction-10) (Kaster et al., 2011). The subsequent two C_1-reduction steps (reactions-4 and 5), are catalyzed by methylene-tetrahydromethanopterin (methylene-H_4MPT) dehydrogenase and methylene-H_4MPT reductase, respectively, and coupled to the redox reaction of coenzyme F_{420}, which is coupled to the H_2/H^+ pair via reaction-9. Reaction-6, the transfer of methyl group from H_4MPT to coenzyme M, is exergonic with an estimated energy yield of –30 kJ/mol. This reaction is coupled to sodium ion translocation to produce sodium motive force for ATP production and reduced ferredoxin (Thauer et al., 2008; Thauer et al., 2010). The last step of methanogenesis, reduction of methyl-coenzyme M (methyl-CoM) to CH_4, is catalyzed by methyl-CoM reductase (MCR) and is another exergonic step in methanogenesis.

2.2 Pathway protein cost model

We apply the pathway protein cost (PPC) model of Flamholz et al. (2013) to hydrogenotrophic methanogenesis. Our model estimates the concentrations of 17 metabolites and cofactors by an optimization algorithm. The cost function (Λ) to minimize is the sum of enzymes (by mass) required for the given pathway flux:

$$\Lambda = \Sigma_{\mathrm{i}} \frac{M_i}{k_{cat,i}} \left(1 + \Pi_j \frac{K_{m,ik}}{C_j}\right) \left(1 - \mathrm{e}^{\frac{\Delta G_{\mathrm{r,i}}}{RT}}\right) \qquad (2)$$

where M_{i} is the molecular mass of an enzyme that catalyzes the reaction i, k_{cat} is a turnover number for the enzyme, $K_{\mathrm{m,ik}}$ is the half saturation constant for the substrate k in reaction i, $\Delta G_{\mathrm{r,i}}$ is the free energy change of the reaction i, R is the gas constant, and T is the temperature in Kelvin (*see* Table 2 for a list of notations and symbols). The first term on the right-hand side of equation-2 represents the base kinetic parameter for enzymes and indicates that less enzyme (by mass) is required if the enzyme has lower molecular weight (M_{i}) or higher turnover rate (k_{cat}). The second term represents an approximate solution for reversible Michaelis-Menten kinetics, which takes into account the penalty when substrate metabolite concentration is lower than the half saturation constant. The third term is derived from the flux-force relationship that relates thermodynamic drive to the ratio of forward (J^+) to backward (J^-) pathway fluxes:

$$\frac{J^+}{J^-} = e^{-\frac{\Delta G_r}{RT}} \qquad . \qquad (3)$$

The third term in equation-2 indicates that when ΔG_r is less negative, higher forward flux (and thus more protein) is required to maintain the same net flux ($J_{net} = J^+ - J^-$). The cost function is the sum of protein costs for all reactions considered (8 in our model, excluding reactions-8 and -9 in Table 1). The cost function, Λ, has a unit of mass of protein per pathway flux (e.g., g-protein s mol^{-1}), and the reciprocal of the cost function $1/\Lambda$ is the pathway flux per protein, that is methane production rate (MPR) per mass of protein (e.g., in mol CH_4 s^{-1} g $protein^{-1}$).

The cost function (equation-2) is optimized under the conditions that all reactions are exergonic ($\Delta G_r < 0$) with metabolite concentrations within upper and lower bounds (Flamholz et al.,2013). Kinetic parameters for enzymes were taken from the literature (Table 3 also *see* Peterson et al.,2014). Enzymes catalyzing reactions-3 and 4, methenyl-H_4MPT^+ cyclohydrolase and methylene-H_4MPT dehydrogenase, respectively, were only assayed in the reverse direction; we took the value for the reverse direction and assumed the same K_m values for corresponding substrates. These kinetic parameters differ by experiments, species, and experimental conditions; the sensitivity of the model for enzyme kinetic parameters are presented in the supplementary material. Upper and lower bounds of metabolites and cofactors are set to 10 mM and 1 nM, respectively, following Wing and Halevy (2014) and Noor et al. (2014), except for the upper bound of H_4MPT and their C_1 compounds (100 mM) because relatively high concentrations were previously reported (Daniels, 1993 and references therein). The upper limit of H_4MPT is related to the lower limit of pH_2 for methanogenesis as we discuss in section 4.1.

The Gibbs free energy change of reactions are listed in Table 1. Reaction-6 is coupled to sodium ion translocation. Based on the growth yield of methanogen without cytochromes for laboratory cultures of *M. marburgensis*, Thauer et al. (2008) estimated an ATP yield of 0.5 mol per mole of CH_4 produced. Assuming the synthesis of ATP from ADP in living cells requires -50 kJ/mol (Thauer et al., 1977), -25 kJ/mol of free energy change of reaction-6 is used for sodium translocation by growing cultures of methanogens. Since it is not clear how much free energy is coupled with Na^+ translocation for reaction-6 under H_2-limited conditions in natural environments, we assumed that half the free energy is used for Na^+ translocation as derived above. The value of ΔG_r for reaction-6 ranges from –32 to –4 kJ/mol for pH_2 100 kPa to 0.14 Pa such that energy used for Na^+ translocation was –16 to –2 kJ/mol in our model. Reactions-8 and -9 are reactions for cofactors and are excluded from the protein cost function (equation-2). The model conditions include $\Delta G_r < 0$ for reaction-9 but reaction-8 can be endergonic (i.e., the Fd_{red}/Fd_{ox} pair is in disequilibrium with the H_2/H^+ pair). The sensitivity of the model was tested by varying one input variable at a time (k_{cat}, K_m, or ΔG_r) and solved for *MPR* and isotopologue compositions of methane (supplementary materials, Figure S1 and S2). Optimization was performed using MATLAB, and the model was run for a range of pH_2 from 0.1 Pa to 100 kPa.

2.3 Estimating the effect of transport limit

The PPC model provides the rate of methanogenesis as a function of thermodynamic driving force gauged by pH_2, a metric that was used in previous experimental studies (e.g., Okumura et al., 2016; Penning et al., 2005). For gases with low solubilities, such as H_2 and CH_4, however, the gas-liquid transfer can limit the rate of microbial growth and metabolisms (e.g., Jud et al., 2007; Pauss et al., 1990; Valentine et al., 2000). Due to the high solubility, dissolution and diffusion of CO_2 are unlikely to limit the rate of methanogenesis for laboratory cultures except for highly alkaline conditions (Miller et al., 2018).

For a bioreactor at steady state, the rate of dissolution equals to H_2 consumption:

$$k_L a(K_H pH_2 - mH_2) = 4\frac{N_{cell}}{V} csMPR \quad (4)$$

where, k_La is the volumetric mass transfer coefficient, N_{cell}/V and *csMPR* are cell density and cell specific *MPR*, respectively (e.g., Pauss et al., 1990). The factor 4 is for reaction stoichiometry of H_2/CH_4 from equation-1. The mass transfer coefficient (k_La) represents the rate of transfer for the whole reactor, and depends upon the stirring rate, bubble size and geometry of the reactor. The value of k_La ranges across orders of magnitude (e.g., Garcia-Ochoa and Gomez, 2005). For example, Pauss et al. (1990) reported a k_La of 0.16 hr^{-1} for a stirred fed-batch anaerobic fermenter, whereas Jud et al., (1997) measured much higher values of 220 to 1500 h^{-1} for a pure culture of methanogen in a 2-L bioreactor.

In addition to gas-liquid transfer rate, diffusion of H_2 in water can limit the rate of methanogenesis in nature and in some co-culture experiments (Hoehler, 2004; Boone et al., 1989). Assuming spherical geometry for a microbe, the concentration gradient to sustain substrate flux (*J*) into the cell can be written as:

$$m_{H2}(x) - m_{H2}(r) = \frac{J}{4\pi D} \cdot \left(\frac{1}{r} - \frac{1}{x}\right) \quad (5)$$

where m_{H2} is the concentration of H_2 at distance *x* and *r* from the center of the cell, *r* is the radius of the cell, *D* is the diffusion coefficient (Hoehler, 2004). Because the mean distance between cells at cell density 10^8 cells/mL is 21 µm, at the high-end of cell density for a culture, *r* is much smaller than *x* for most conditions in cultures and nature. Equation-5, thus, can be reduced to

$$\Delta m_{H2} = \frac{J}{4\pi D} \cdot \left(\frac{1}{r}\right) \quad (6)$$

where Δm_{H2} is the concentration gradient between the bulk media or porewater and the surface of the cell.

2.4 Isotopologue flow network model applied to methanogenesis

Based on the biochemical pathway of methanogenesis described in the previous sections, a mathematical model was constructed to quantitatively describe the isotope fractionations of microbial methanogenesis. The isotope flow network model was originally developed to explain sulfur isotope fractionation by sulfate reducing microbes (Rees, 1973), which was later modified by a number of studies (Brunner and Bernasconi, 2005; Farquhar et al., 2003; Wing and Halevy, 2014). A similar model was also applied for carbon isotope fractionations within biosynthetic pathways (e.g., Hayes, 2001), as well as isotopologue fractionations during methanogenesis (Yoshinaga et al., 2014; Wang et al., 2015; Stolper et al., 2015, Cao et al., 2019) and anaerobic methane oxidation (Ono et al.2021; Wegener et al., 2021). We note that Wing and Halevy (2014) was the first study that linked Gibbs free energy of reaction to the reversibilities and applied it to the isotope flow network model.

These isotope flux network models use prescribed kinetic isotope effects (KIEs) intrinsic to each enzymatic reaction and calculates isotope fractionations of the overall pathway as a function of reaction reversibilities that maintain isotopologue mass balance. Application of flow network model to the carbon isotope system of methanogenesis is straightforward; its application to singly- or doubly-deuterated isotopologues, however, is complicated due to

molecular symmetry and multiple sites where D can substitute H. Our approach is to set up a total of 26 isotopologue mass balance equations (8 for ^{13}C, 7 each for ^{12}CD and ^{13}CD, and 4 for D_2 isotopologues). Since these can be arranged in a set of linear equations, we use matrix algebra to simultaneously solve for the isotopologue compositions of methane as well as the isotopologue compositions of all intermediates as described below.

2.4.1 Notations

Notations and symbols used in this study are summarized in Table 2. In this paper, r_j, d_j, q_j, *and* u_j represent the abundance ratios of ^{13}C, D, ^{13}CD, and D_2 substituted isotopologues relative to ^{12}C-H containing isotopologues, respectively, and j is an index of single carbon containing species (j=1 to 8) in Table 4.

For example,

$$r_8 = \frac{^{13}CH_4}{^{12}CH_4}\,,\ d_8 = \frac{^{12}CH_4D}{^{12}CH_4}\,,\ q_8 = \frac{^{13}CH_4D}{^{12}CH_4}\,,\ u_8 = \frac{^{12}CH_2D_2}{^{12}CH_4} \qquad (7)$$

Isotope ratios are then described using conventional delta notations:

$$\delta^{13}C = \frac{r_i}{r_{ref}} - 1\ \text{, and}\ \delta D = \left(\frac{^{x}\sigma_j}{\sigma_j}\right)\frac{d_j}{d_{ref}} - 1 \qquad (8)$$

where r_{ref} and d_{ref} denote the isotope ratios of reference materials. For this study, r_{ref} is the $^{13}C/^{12}C$ ratio of CO_2, and d_{ref} is the D/H ratio of H_2O. We use H_2O as a reference because it is commonly measured for environmental studies and most H carriers are exchangeable with H in H_2O (*see* section 2.4.2). The symmetry ratio ($^{x}\sigma_j/\sigma_j$) is used to calculate isotope ratios from isotopologue ratios for deuterated species. For example, the symmetry ratios for singly-deuterated methane ($^{12}CH_3D$ and $^{13}CH_3D$) are 1/4 based on the symmetry number of CH_3D ($^{d}\sigma_8 = 3$) over CH_4 ($\sigma_8 = 12$). The symmetry number for doubly-deuterated methane ($^{12}CH_2D_2$) is 2 such that the symmetry ratio is 1/6 for $^{12}CH_2D_2/^{12}CH_4$.

The abundance of clumped isotopologues ($^{13}CH_3D$ and $^{12}CH_2D_2$) is quantified by the metrics $\Delta^{13}CD$ and ΔD_2, which are the deviations of the ratios $^{13}CD/^{12}CH$ and $^{12}CD_2/^{12}CH_2$ relative to those expected for stochastic abundance:

$$\Delta^{13}CD_j = \frac{q_j}{r_j d_j} - 1\ \text{and}\ \Delta DD_j = \frac{(^{u}\sigma_j/\sigma_j)}{(^{d}\sigma_j/\sigma_j)^2}\frac{u_j}{d_j^2} - 1 \qquad (9)$$

Kinetic isotope effect (KIE) is defined as the ratio of rate constants for a given isotopologue against ^{12}C-H isotopologue. For example, $\alpha_i = {}^{13}k_i/{}^{12}k_i$. where, $^{x}k_i$ is the rate constant for isotopologue x for reaction i (Table 2; Table 1). We consider both primary (α_{pi}) and secondary (α_{si}) KIEs for deuterated isotopologues. Primary fractionation occurs when a C–D bond is broken or formed, whereas secondary fractionation occurs during a reaction in which a C–D bond (or two C–D bonds) is(are) transferred from a reactant to a product while breaking or forming a C–H bond (*see* Table 5).

KIEs for multiply-substituted (clumped) isotopologues follows the rule of geometric mean (Bigeleisen, 1955) such that the KIE for $^{13}CH_3D$, for example, is approximately the product of KIEs for D/H and $^{13}C/^{12}C$. A small deviation from this rule is expected due to combined zero-point

energy shifts for double substitutions (Whitehill et al., 2017), and it is quantified by the γ_x factor (Table 2) (Wang et al., 2015). For example:

$$\alpha^{+}_{\mathrm{cp7}} = \gamma_{\mathrm{cp7+}}\ \alpha^{+}_{7}\ \alpha^{+}_{\mathrm{p7}} \quad (10)$$

Table 5 shows 8 isotopologue reactions considered for the last step of methanogenesis (reaction-7). Note the symmetry factors of ¼ and ¾ for the reverse reaction for primary and secondary D-abstraction reactions, respectively. These are derived from reaction symmetry (e.g., Bigeleisen, 1949) but related to a statistical chance to remove D or H from $^{12}CH_3D$ (or $^{13}CH_3D$). For solving the isotope flow network model, we did not consider reactions for doubly-substituted isotopologues for the mass balance of singly-substituted isotopologues. For example, a reaction, CH_2D_2 + R → CH_2D-R + D, was not included in the mass balance for singly-deuterated isotopologues. The result is accurate because of the relatively low abundance of doubly-substituted compared to singly-substituted isotopologues.

2.4.2 Isotopologue flow network model

The isotopologue flow network model tracks the flow of isotopologues among 8 metabolites from CO_2 to CH_4 (Table 4). We set up a total of 26 mass balance equations (8 for ^{13}C, 7 for D and ^{13}CD, and 4 for D_2-substituted isotopologues). These mass balance equations are used to construct a fractionation matrix ***F***, which is solved by using matrix algebra for the isotopologue ratios of CH_4 as well as all intermediates. In this study, the fractionation matrix ***F*** was constructed manually but it can be automatically generated for a model with larger and more complex molecules (*see* Goldman et al., 2019 for ^{13}C models).

Each reaction (reactions-1 to 7) is given forward and backward fluxes (e.g., the number of moles of substrates per cell per unit time), which are denoted as J_i^+ and J_i^-, respectively (i = 0 to 7). Reversibility (ϕ_i) is defined as: $\phi_i = J_i^-/J_i^+$. Assuming intermediate steady states, net fluxes are equal to the difference between forward and reverse fluxes (i.e., $J_{net} = J_0^+ - J_0^- = J_1^+ - J_1^- = \ldots = J_8^+$) such that all J_n^+ and J_n^- terms can be solved as a function of ϕ_i and J_{net}:

$$J_i^+ = \frac{1}{1-\phi_i} J_{net} \text{ , and } J_i^- = \frac{\phi_i}{1-\phi_i} J_{net} \ , \quad (11)$$

When solving for a steady state, J_{net} cancels out so that the model solution only depends on the reversibility (ϕ_1 to ϕ_7) and does not depend on the rate of methanogenesis.

For ^{13}C isotopologues, a series of mass balance equations can be written as:

$$\frac{d^{13}m_1}{dt} = J_0^+ r_0 - (\alpha_1^+ J_1^+ + J_0^-) r_1 + \alpha_1^- J_1^- r_2 \quad (12a)$$

$$\frac{d^{13}m_2}{dt} = \alpha_1^+ J_1^+ r_1 - (\alpha_2^+ J_2^+ + \alpha_1^- J_1^-) r_2 + \alpha_2^- J_2^- r_3 \quad (12b)$$

$$\frac{d^{13}m_3}{dt} = \alpha_2^+ J_2^+ r_2 - (\alpha_3^+ J_3^+ + \alpha_2^- J_2^-) r_3 + \alpha_3^- J_3^- r_4 \quad (12c)$$

$$\ddots$$

$$\frac{d^{13}m_7}{dt} = \alpha_6^+ J_6^+ r_6 - (\alpha_7^+ J_7^+ + \alpha_6^- J_6^-) r_7 + \alpha_7^- J_7^- r_8 \quad (12c)$$

$$\frac{d^{13}m_8}{dt} = \alpha_7^+ J_7^+ r_7 - (\alpha_8^+ J_8^+ + \alpha_7^- J_7^-) r_8 \quad (12d)$$

where $^{13}m_j$ is the amount (e.g., mol) of ^{13}C-isotopologues *in vivo*, and r_0 is the $^{13}C/^{12}C$ ratio of CO_2 outside the cell. Assuming intermediate steady states (i.e., $d^{13}m_j/dt = 0$), a set of linear equations (equations-12a to 12d) can be arranged into a tridiagonal matrix ***F***. Equation-12 shows the relationship among ***F***, an isotopologue ratio column vector ***r***, and a boundary condition column vector ***b*** as ***F*** ·***r*** = ***b***:

$$\begin{bmatrix} \alpha_1^+ J_1^+ + J_0^- & -\alpha_1^- J_1^- & & & & \\ -\alpha_1^+ J_1^+ & \alpha_2^+ J_2^+ + \alpha_1^- J_1^- & -\alpha_2^- J_2^- & & & \\ & -\alpha_2^+ J_2^+ & \ddots & \ddots & & \\ & & \ddots & \ddots & & \\ & & & -\alpha_7^+ J_7^+ & \alpha_8^+ J_8^+ + \alpha_7^- J_7^- \end{bmatrix} \begin{bmatrix} r_1 \\ r_2 \\ r_3 \\ \ddots \\ r_8 \end{bmatrix} = \begin{bmatrix} J_0^+ r_0 \\ 0 \\ 0 \\ \ddots \\ 0 \end{bmatrix} \quad (13)$$

Equation-13 can be solved for the carbon isotopologue ratios of all intermediate species (r_j) by inverting the fractionation matrix (***r*** = $\boldsymbol{F}^{-1}\boldsymbol{b}$).

Mass conservations for deuterated isotopologues are more complicated than ^{13}C due to primary and secondary KIEs and reaction symmetry factors for reverse (bond-breaking) reactions:

$$\frac{d^2m_2}{dt} = \alpha_{p1}^+ J_1^+ d_{\mathrm{H}} - (\alpha_{p1}^- J_1^- + \alpha_{s2}^+ J_2^+) d_2 + \alpha_{s2}^- J_2^- \, d_3 \quad (14a)$$

$$\frac{d^2m_3}{dt} = \alpha_{s2}^+ J_2^+ d_2 - (\alpha_{s2}^- J_2^- + \alpha_{s3}^+ J_3^+) d_3 + \alpha_{s3}^- J_3^- \, d_4 \quad (14b)$$

$$\frac{d^2m_4}{dt} = \alpha_{s3}^+ J_3^+ d_3 - (\alpha_{s3}^- J_3^- + \alpha_{s4}^+ J_4^+) d_4 + \alpha_{s4}^- J_4^- \, d_5 \quad (14c)$$

$$\frac{d^2m_5}{dt} = \alpha_{p4}^+ J_4^+ d_{\mathrm{H}} + \alpha_{s4}^+ J_4^+ d_4 - (\tfrac{1}{2}\alpha_{p4}^- J_4^- + \tfrac{1}{2}\alpha_{s4}^- J_4^- + \alpha_{s5}^+ J_5^+) d_5 + \alpha_{s5}^- J_5^- \, d_6 \quad (14d)$$

$$\frac{d^2m_6}{dt} = \alpha_{p5}^+ J_5^+ d_{\mathrm{H}} + \alpha_{s5}^+ J_5^+ d_5 - (\tfrac{1}{3}\alpha_{p5}^- J_5^- + \tfrac{2}{3}\alpha_{s5}^- J_5^- + \alpha_{s6}^+ J_6^+) d_6 + \alpha_{s6}^- J_6^- \, d_7 \quad (14e)$$

$$\frac{d^2m_7}{dt} = \alpha_{s6}^+ J_6^+ d_6 - (\alpha_{s6}^- J_6^- + \alpha_{s7}^+ J_7^+) d_7 + \alpha_{s7}^- J_7^- \, d_8 \quad (14f)$$

$$\frac{d^2m_8}{dt} = \alpha_{p7}^+ J_7^+ d_{\mathrm{H}} + \alpha_{s7}^+ J_7^+ d_7 - (\tfrac{1}{4}\alpha_{p7}^- J_7^- + \tfrac{3}{4}\alpha_{s7}^- J_7^- + J_8^+) d_8 \quad (14g)$$

where, d_{H} is the D/H ratio of source H. We assumed H source is water, as most H carriers (e.g., HS in methyl-coM, H in $F_{420}H_2$) are exchangeable with H in water. For example, during reaction-4, H added to CH_2=H_4MPT is derived from C5 position of $F_{420}H_2$ (Klein and Thauer, 1995), which is derived from H_2O and not from H_2 as is written in reaction-9 (Livingston et al., 1987). We note that at least one hydrogenase, H_2-forming methylene-H_4MPT dehydrogenase, has been shown to directly transfer H_2 in H during the reduction of methenyl- to methylene-H_4MPT (Zirngible et al., 1992). The enzyme is upregulated during early growth phase (Nolling et al., 1995) or under conditions of excess H_2 (Morgan et al., 1997; Hendrickson et al., 2007) and may explain some experimental results (Kawagucci et al., 2014).

Again, the series of equations-13a to 13g can also be arranged in a matrix form:

$$\begin{bmatrix} \alpha_{p1}^- J_1^- + \alpha_{s2}^+ J_2^+ & -\alpha_{s2}^- J_2^- & & & & \\ -\alpha_{s2}^+ J_2^+ & \alpha_{s2}^- J_2^- + \alpha_{s3}^+ J_3^+ & -\alpha_{s3}^- J_3^- & & & \\ & -\alpha_{s3}^+ J_3^+ & \ddots & \ddots & & \\ & & \ddots & \ddots & & \\ & & & \alpha_{s7}^+ J_7^+ & \tfrac{1}{4}\alpha_{p7}^- J_7^- + \tfrac{3}{4}\alpha_{s7}^- J_7^- + J_8^+ \end{bmatrix} \begin{bmatrix} d_2 \\ d_3 \\ d_4 \\ \ddots \\ d_8 \end{bmatrix} = \begin{bmatrix} \alpha_{p1}^+ J_1^+ d_H \\ 0 \\ 0 \\ \ddots \\ \alpha_{p7}^+ J_7^+ d_{\mathrm{H}} \end{bmatrix} \quad (15)$$

and solved by inverting the fractionation matrix for the values of d_j (j=2 to 8).

For ^{13}C-D isotopologues, mass balance equations are similar to singly-deuterated isotopologues and solved similarly.

$$\frac{d^{13,2}m_2}{dt} = \alpha^+_{cp1} J^+_1 r_1 d_{\mathrm{H}} - (\alpha^-_{cp1} J^-_1 + \alpha^+_{cs2} J^+_2) q_2 + \alpha^-_{cs2} J^-_2\ q_3 \quad (16a)$$

$$\frac{d^{13,2}m_3}{dt} = \alpha^+_{cs2} J^+_2 q_2 - (\alpha^-_{cs2} J^-_2 + \alpha^+_{cs3} J^+_3) q_3 + \alpha^-_{cs3} J^-_3\ q_4 \quad (16b)$$

$$\frac{d^{13,2}m_4}{dt} = \alpha^+_{cs3} J^+_3 q_3 - (\alpha^-_{cs3} J^-_3 + \alpha^+_{cs4} J^+_4) q_4 + \alpha^-_{cs4} J^-_4\ q_5 \quad (16c)$$

$$\frac{d^{13,2}m_5}{dt} = \alpha^+_{cp4} J^+_4 r_4 d_{\mathrm{H}} + \alpha^+_{cs4} J^+_4 q_4 - (\tfrac{1}{2}\alpha^-_{cp4} J^-_4 + \tfrac{1}{2}\alpha^-_{cs4} J^-_4 + \alpha^+_{cs5} J^+_5) q_5 + \alpha^-_{cs5} J^-_5\ q_6 \quad (16d)$$

$$\frac{d^{13,2}m_6}{dt} = \alpha^+_{cp5} J^+_5 r_5 d_{\mathrm{H}} + \alpha^+_{cs5} J^+_5 q_5 - (\tfrac{1}{3}\alpha^-_{cp5} J^-_5 + \tfrac{2}{3}\alpha^-_{cs5} J^-_5 + \alpha^+_{cs6} J^+_6) q_6 + \alpha^-_{cs6} J^-_6\ q_7 \quad (16e)$$

$$\frac{d^{13,2}m_7}{dt} = \alpha^+_{cs6} J^+_6 q_6 - (\alpha^-_{cs6} J^-_6 + \alpha^+_{cs7} J^+_7) q_7 + \alpha^-_{cs7} J^-_7\ q_8 \quad (16f)$$

Double deuterium substitutions only apply to four species (j=5 to 8 in Table 4; CD_2=H_4MPT to CH_2D_2), and their mass conservation equations are:

$$\frac{d^{2,2}m_5}{dt} = \alpha^+_{dp4} J^+_4 d_4 d_{\mathrm{H}} - (\alpha^-_{dp4} J^-_4 + \alpha^+_{ds5} J^+_5) u_5 + \tfrac{1}{3}\alpha^-_{ds5} J^-_5\ u_6 \quad (17d)$$

$$\frac{d^{2,2}m_6}{dt} = \alpha^+_{dp5} J^+_5 d_5 d_{\mathrm{H}} + \alpha^+_{cs5} J^+_5 u_5 - (\tfrac{2}{3}\alpha^-_{dp5} J^-_5 + \tfrac{1}{3}\alpha^-_{ds5} J^-_5 + \alpha^+_{ds6} J^+_6) u_6 + \alpha^-_{ds6} J^-_6\ u_7 \quad (17e)$$

$$\frac{d^{2,2}m_7}{dt} = \alpha^+_{ds6} J^+_6 u_6 - (\alpha^-_{ds6} J^-_6 + \alpha^+_{ds7} J^+_7) u_7 + \alpha^-_{ds7} J^-_7\ u_8 \quad (17f)$$

$$\frac{d^{2,2}m_8}{dt} = \alpha^+_{dp7} J^+_7 d_7 d_{\mathrm{H}} + \alpha^+_{ds7} J^+_7 u_7 - (\tfrac{1}{2}\alpha^-_{dp7} J^-_7 + \tfrac{1}{2}\alpha^-_{ds7} J^-_7 + \alpha^+_{ds8} J^+_8) u_8 \quad (17g)$$

These can be arranged in a matrix form:

$$\begin{bmatrix} \alpha^-_{dp4} J^-_4 + \alpha^+_{ds5} J^+_5 & -\tfrac{1}{3}\alpha^-_{ds5} J^-_5 & & \\ -\alpha^+_{cs5} J^+_5 & \tfrac{2}{3}\alpha^-_{dp5} J^-_5 + \tfrac{1}{3}\alpha^-_{ds5} J^-_5 + \alpha^+_{ds6} J^+_6 & -\alpha^-_{ds6} J^-_6 & \\ & -\alpha^+_{ds6} J^+_6 & \alpha^-_{ds6} J^-_6 + \alpha^+_{ds7} J^+ & -\alpha^-_{ds7} J^-_7 \\ & & -\alpha^+_{ds7} J^+_7 & \tfrac{1}{2}\alpha^-_{dp7} J^-_7 + \tfrac{1}{2}\alpha^-_{ds7} J^-_7 + \alpha^+_{ds8} J^+_8 \end{bmatrix} \begin{bmatrix} u_5 \\ u_6 \\ u_7 \\ u_8 \end{bmatrix} = \begin{bmatrix} \alpha^+_{dp4} J^+_4 d_4 d_{\mathrm{H}} \\ \alpha^+_{dp5} J^+_5 d_5 d_{\mathrm{H}} \\ 0 \\ \alpha^+_{dp7} J^+_7 d_7 d_{\mathrm{H}} \end{bmatrix} \quad (18)$$

The resulting isotopologue ratios (r_j, d_j, q_j, and u_j) are used to calculate isotope ratios (δ^{13}C and δD) and clumped isotopologue compositions (Δ^{13}CD and ΔD_2) following equations-8 and 9.

2.4.3 Assignment of KIE values

The magnitudes of KIEs are key input parameters for the isotopologue flow network model. While experimental data or theoretical estimates for KIEs of enzymatic reactions are limited, equilibrium fractionation factors estimated by quantum mechanical calculation (Ono et al., 2021; Gropp et al., 2020) are considered to be accurate for the purpose of this work. The knowledge of equilibrium fractionation factors constrains the model solution for the fully reversible (equilibrium) case. We used equilibrium fractionation factors estimated by Gropp et al. (2020) for fractionations among metabolites against water vapor and gaseous CO_2. Experimentally derived fractionation factors between liquid water and vapor water by Horita and Wesolowski (1994) were used to derive equilibrium fractionation factors against liquid water. We are aware of other fractionation factors (e.g., Horibe and Craig, Turner et al., 2021 for CH_4-

H_2O, Kueter et al., 2019 and Horita 2001 for CH_4-CO_2) but we did not use them to keep consistency. Table 4 lists isotopologue compositions (in δ and Δ values) of all metabolites expected under equilibrium at 25°C. We used 25°C for our model calculation to be consistent with thermodynamic data by Thauer et al. (2008). The model sensitivity of temperature of fractionation is presented in supplementary materials (Figure S3). The estimated equilibrium carbon isotope compositions systematically decrease with decreasing carbon oxidation state. Clumped isotope fractionations are largely constant at 5.0 ± 0.8‰ and 16.0 ± 2.6‰, for $\Delta^{13}CD$ and ΔD_2, respectively (Table 4).

Once KIE for the forward reaction is assigned, KIE for the reverse reaction is constrained by the equilibrium fractionation factors (and vice versa). This maintains consistency and effectively reduces the number of input parameters to half. For example, for reaction-7:

$$\alpha_{p7}^{eq} = \frac{d_H}{d_8} = \frac{\alpha_{p7}^{-}}{\alpha_{p7}^{+}} \quad (19)$$

and

$$\alpha_{s7}^{eq} = \frac{d_7}{d_8} = \frac{\alpha_{s7}^{+}}{\alpha_{s7}^{-}} \quad (20)$$

where, α_{pj}^{eq} and α_{sj}^{eq}, represent equilibrium fractionation factors for primary and secondary fractionations, respectively.

Similarly, the following relationships apply for clumped KIEs:

$$\gamma_8 = \frac{\gamma_{p7}^{-}}{\gamma_{p7}^{+}}, \text{ and } \frac{\gamma_7}{\gamma_8} = \frac{\gamma_{s7}^{-}}{\gamma_{s7}^{+}} \quad (21)$$

To our knowledge, Scheller et al., (2013) is the only study that examined the enzyme isotope effect associated with methanogenesis *in vitro*. The values of KIEs for other reactions are the major uncertainty for the isotopologues flow network model. We assigned KIEs with a range of uncertainty and propagated to the product isotopologue ratios by the Monte Carlo simulation (*N*=1000) assuming normal distribution with 1σ values listed in Table 6 (*N*=1000). Scheller et al. (2013) reported ^{13}C-KIE of 0.96±0.01 for reaction-7 (formation of methane from CH_3-S-CoM and HS-CoB) assayed at 60°C. For simplicity, ^{13}C-KIEs for forward reactions are assumed to be 0.96±0.02 except for the last step, to which we assigned a smaller uncertainty of ±0.01 (Table 6). By using the same magnitude of KIEs, we aim to examine the isotopologues fractionation due to differential reversibility. These yield ^{13}C-KIEs of backward reactions ranging from 0.957 to 0.977 (Table 6). For comparison, ^{13}C-KIEs were experimentally determined to be 0.96 for yeast formate dehydrogenase (formate to CO_2) and 0.98 for alcohol dehydrogenase (alcohol to aldehyde) (Hermes et al., 1984; Scharshmidt et al., 1984).

Scheller et al (2013) reported a primary KIE (k_H/k_D) of 2.44 ± 0.22 for the activation of methane (note that enzyme community reports KIEs by H/D); the reciprocal of this value yields a α_{p7}^{-} value of 0.41 ± 0.04. This yields a forward primary D-KIE (α_{p7}^{+}) of 0.34 based on the equilibrium fractionation factor between CH_4 and $H_2O_{(l)}$ of 0.822 (Table 6). This magnitude of primary isotope effect is commonly observed during the breaking or forming of C–D/C–H bonds. For reference, primary D-KIE of 0.24 is measured for yeast alcohol dehydrogenase (Cha et al., 1989) and that of 0.46 is reported for formate dehydrogenase (Hermes et al., 1984). Bell (1973) estimated the minimum value of 0.15 for D-KIE of C–D/C–H bond-breaking reactions (i.e., α_p^{-})

based on a typical zero-point energy difference between C-D and C-H asymmetric stretching vibrations of 4.8 kJ/mol (ca. 400 cm^{-1}). We assigned 0.82±0.20 for the D-primary KIEs in reverse directions (α_{pi}-) for reactions 1, 4 and 6 as the best fit to the experimental data; these D-KIEs are the least constrained variable in the model.

For secondary D-KIE, Scheller et al. (2013) report 0.84 and 0.85 for forward and backward reactions, respectively, for the reaction-7. Accordingly, we assigned 0.85±0.05 for all forward secondary D-KIEs (α_{si}^{+}), except for the last step with a smaller uncertainty of ±0.01, and derived backward D-KIEs from equation-20 (Table 6). For comparison, Roston and Kohen (2010) reported secondary D-KIE associated with the alcohol dehydrogenase of 0.94 for the forward reaction (alcohol to aldehyde) and 0.81 for the reverse reaction.

It is worth noting that clumped KIEs for enzyme reactions have been previously studied by comparing $^{13}C/^{12}C$ fractionation of deuterated versus non-deuterated substrates (summarized in Rucker and Klinman, 1999). For example, the ^{13}C-KIE is 0.9853 for the oxidation of benzyl alcohol catalyzed by alcohol dehydrogenase and the KIE increases to 0.9788 for doubly-deuterated benzyl alcohol-α,α-d_2 (Scharschmidt et al., 1984). These values yield clumped KIE of 0.9933 ($\ln\gamma_p^{-}$ = –6.7‰) for the C–D bond-breaking reaction (note that this was a doubly-deuterated carbon). Accordingly, we assigned 1.000±0.008 for primary clumped KIE (γ_{cp}^{+}). This range of values reproduces the negative (anti-clumped) $\Delta^{13}CH_3D$ values measured for laboratory cultures of methanogens as well as some natural methane samples (Gruen et al.,2018; Wang et al.,2015; Stolper et al.,2015) (Table 7). For doubly-deuterated species, we assigned 1.000±0.010 for primary clumped KIEs (γ_{dp}^{+}) for forward reactions. We also assumed no clumped KIEs for secondary reactions for the forward directions (γ_{cs}^{+}=1.000 and γ_{ds}^{+}=1.000) (Table 7). It is possible that clumped KIEs are associated with secondary D-KIE. Our model can be used to test the isotopologue systematics for different prescribed clumped KIE values, when more experimental data become available.

3 Results

3.1 Differential energy yields and reversibility for methanogenesis reactions

The PPC model allows us to estimate how the free energy of the total methanogenesis reaction (equation-1) is shared among the 8 reactions in the pathway of methanogenesis. Figure 2 shows the model results for cumulative free energy changes for the 8 reactions. The PPC model indicates that reactions-1, 6, 7 and 10 are more exergonic (energy-yielding) than reactions-2, 3, 4, and 5 ($\Delta G_r > -5$ kJ/mol), and this translates to the high pathway fluxes in both directions (high reversiblities) for the middle steps (steps between $CH{\equiv}H_4MPT^{+}$ and CH_3-H_4MPT) of the methanogenesis pathway under the range of pH_2 (0.16 Pa to 100 kPa) that allows methanogenesis (Figure 2; Figure 3). The PPC model suggests that reaction-1 is moderately exergonic. This is partly because the reaction is coupled to an exergonic electron bifurcation reaction (reaction-10) that produces reduced ferredoxin (Figure 1).

The relatively low energy yields ($\Delta G_r > -5$ kJ/mol) for reactions-2 to 5 translate to their high reversibilities ($\varphi > 0.1$) and their relatively high pathway fluxes and protein costs. Since the second and third H atoms are added to C during reactions-2 to 5, their high reversibilities have important effects for isotope systematics. High pathway fluxes (and high protein costs) become significant at lower pH_2 between 1 and 50 Pa, in particular (Figure 3). This is consistent with a

transcriptomics study that reported up-regulation of methylene-H_4MPT dehydrogenase and methylene-H_4MPT reductase for *M. maripaludis* cultured at H_2-limiting conditions (Costa et al., 2013). The last two steps (reactions-6 and 7) are highly exergonic except under very low pH_2 (< 0.6 Pa or mH_2 < 5 nM) when reactions become moderately reversible (φ_6 and φ_7 > 0.1, ΔG_r > –5.7 kJ/mol) (Figure 3). This differential reversibility explains the different pH_2 sensitivity of $\delta^{13}C$ and δD fractionations during microbial methanogenesis, as discussed in section 4.2.

3.2 Methane production rate and H_2 transport limit

The PPC model can be used to model methane production rate (MPR) as a function of pH_2 because the reciprocal of the cost function is pathway flux (J_{net} = MPR) per mass of protein (Figure 4, solid blue line). The result shows a maximum MPR of 133 mmol g-protein^{-1} hour^{-1}. Approximately 10% of the dry weight of cells (DWC) is composed of proteins used for methanogenesis, given that the total protein fraction per biomass is 63% (Peterson et al., 2014) and that 18% of the proteome is associated with methanogenesis (Müller et al., 2021). This yields a maximum MPR of 13 mmol CH_4 g-DWC^{-1} h^{-1}. The modeled MPR is lower compared to MPR of 110 mmol CH_4 g-DWC^{-1} h^{-1} for batch cultures of the mesophilic methanogen, *M. maripaludis* (Goyal et al.,2015), suggesting the model overestimated the protein cost by a factor of 8.

Figure 4 shows the results of calculations including the considerations for dissolution (green lines) and diffusion (red line) limits of H_2 transport. The diffusion limit calculation predicts undersaturation by a factor of 10 or higher, and the dissolution limit calculation predicts undersaturation by a factor of 10 to 1000 for a range of k_La values of 10 to 1000 h^{-1}. The model shows an apparent half saturation constant for methanogenesis at pH_2 at 5 Pa (= $10^{0.7}$ Pa) when the transport limit is not considered (Figure 4; blue line). The dissolution limit with k_La = 100 h^{-1} gives apparent K_m values of 1 kPa, which matches with 670 to 1700 Pa ($10^{2.8}$ to $10^{3.2}$ Pa) measured for laboratory cultures of methanogens (Zinder, 1993 and reference therein) (Figure 4). The lower H_2 threshold for methanogen cultures ranges from 23 to 390 nM (3 to 52 Pa, Cord-Ruwisch et al., 1988). The dissolution limit result of k_La > 100 h^{-1} produced by our model is consistent with these experimental observations (Figure 4).

3.3 Isotopologue fractionations

The model predicts that methane isotopologue fractionations generally follow the patterns for MPR and that isotopologue systematics can be divided into high (≳1 kPa), medium (1k to 10 Pa) and low (<10 Pa) pH_2 regions (Figure 5). The exact pH_2 values depend upon the cell density and k_La values for the reactor set up according to equation-4. The model produced larger ranges of solutions for all four isotopologue compositions at high pH_2 (≳1 kPa) relative to low pH_2 (≲1 kPa) (Figure 5). These larger uncertainties reflect the relatively large uncertainties assigned for the fractionation factors for reaction 1 to 6 (Table 6). The model solution range is better constrained at low pH_2, where KIEs for the reaction-7 are expressed (Figure 5).

The model shows that the magnitude of carbon isotope fractionation is mainly controlled by the reversibility of the first step (reaction-1, Table 1) and increases from –40 to –80‰ as pH_2 decreases from 1 kPa to <10 Pa, reproducing observations for laboratory cultures when a range of fractionation factors are considered (Figure 5A). At high pH_2 (≳1 kPa), the model predicts that all C_1 metabolites except for CH_4 have $\delta^{13}C$ of 0 to 5‰. This indicates that, with prescribed KIE of

0.96, all the fluxes (J_1^+ to J_8^+) carry C with $\delta^{13}C$= –40 to –35‰, including the final product CH_4 (Figure 3). This is because no C enters or leaves the cell except via reaction-1 such that ^{13}C of all the metabolites are predominantly controlled by KIE of the first irreversible step (α_1^+) of 0.96 (Table 6). When the first step (J_1^+) becomes reversible at lower pH_2 between 1 kPa to 10 Pa, the increased reversibility allows additional KIEs during reactions-6 and -7 to be expressed to produce maximum fractionations down to -80‰. At very low pH_2 below 10 Pa, $\delta^{13}C$ value of methane increases and approaches to equilibrium value of -66.3‰ because the last two reactions become reversible (Table 4; Figure 5).

In contrast to $\delta^{13}C$ value of methane, which is sensitive to the reversibility of the whole pathway, δD value of methane is mainly controlled by the last reversible step. This is because the last reversible primary-D reaction resets the D/H fractionation for upstream reactions by exchanging isotopes with water.

At high pH_2 above 1kPa, δD values of-360±80‰ correspond to the kinetic endmember. A large range of model solutions reflect the relatively large uncertainty (±200‰ 1σ) assigned for the primary D-fractionation factors for the first three H-addition reactions (Table 6). The model solutions show a relatively narrower range of ±80‰ (for 67 percentile) compared to model inputs of ±200‰ because of the averaging over the four hydrogens (the error for the average of 4 numbers is 1/√4).

At lower pH_2 from 10 Pa to 1 kPa, the reversibility for reaction-5 increases and CH_4 shows relatively constant δD values of –340±40‰ (Figure 5B). This explains the observation by Okumura et al. (2016) of relatively constant D/H fractionation under a range of pH_2 at fractionation of -320 ± 10‰ (albeit 20‰ higher than our model prediction). At this pH_2 range (10 Pa to 1 kPa), three H atoms in methane carry near-equilibrium signals (Figure 3-B and C). Fully equilibrated CH_3-CoM would have δD of –131‰ (Table 4). The addition of a highly D-depleted fourth H atom ($1-\alpha_{p7}^+$= –620‰) can explain the commonly observed fractionation of –300 ± 40‰ between H_2O and CH_4 (Figure 5; Ono et al., 2021). At pH_2 <10 Pa, the last reaction becomes reversible and δD values approach the equilibrium value of –178‰, although full equilibrium is not attained in the model.

Doubly-substituted isotopologues follow complicated patterns with $\Delta^{13}CH_3D$ and $\Delta^{12}CH_2D_2$ values reflecting kinetic versus equilibrium end-members as well as the effect of mixing (Figure 5C and 5D). A wide range of $\Delta^{13}CH_3D$ at pH_2 above 1 kPa predicted by the model (–3.8 to 4.5‰) is consistent with a wide range of $\Delta^{13}CH_3D$ values (–4.7 to 6.2‰) reported for laboratory cultures of methanogens. The range for solutions is less than the assigned uncertainty for γ_{cp}^+ values (±8‰) because of the averaging effect (Table 7). The model also predicts a wide range of $\Delta^{12}CH_2D_2$ values. At high pH_2 (>1kPa), the model predicts highly negative $\Delta^{12}CH_2D_2$ of -25‰ for the default case and down to –50‰ due to combinatorial effects (Yeung, 2016; Röckmann et al., 2016).

Figure 6 shows the cross-plot of isotopologue ratios. It shows the trajectory of kinetic ($\delta^{13}C$ =-40, δD=-360‰) to equilibrium endmembers ($\delta^{13}C$ = -66‰ and δD=-178‰). For all isotopologues, model uncertainties become larger for kinetic end-members than equilibrium end-members because of the smaller uncertainty for KIEs for the last step of methanogenesis (reaction-7).

4 Discussion

4.1 Metabolite (CH_3-H_4MPT) concentration limits the rate of methanogenesis at low pH_2

The protein cost model predicts that the lower bound concentration of CH_3-H_4MPT limits the rate and thermodynamic feasibility of methanogenesis. Figure 7 compares the predicted metabolite concentrations at pH_2 of 100 Pa and 1 Pa, showing the low concentration of CH_3-H_4MPT at low pH_2 conditions. This is because reactions-4 and 5 (reductions of $CH{\equiv}H_4MPT^+$ to $CH_2{=}H_4$MPT and $CH_2{=}H_4$MPT to CH_3-H_4MPT) are both coupled to the redox of cofactor $F_{420}/F_{420}H_2$ (standard mid potential, $E^{0\prime}$ = –356 mV) (Figure 1; Table 1). The redox potential of the H_2/H^+ pair becomes less negative and increases from –413 mV to –265 mV, as pH_2 decreases from 100 kPa to 1 Pa. In order to accept electrons from $F_{420}H_2$, the concentration ratios of $CH{\equiv}H_4MPT^+/CH_2{=}H_4$MPT ($E^{0\prime}$ = –387 mV) and $CH_2{=}H_4MPT/CH_3$-H_4MPT ($E^{0\prime}$ = –325 mV) have to increase (i.e., redox potentials become less negative). Accordingly, the lowest pH_2 at which methanogenesis can proceed depends upon the dynamic range (upper and lower bound concentrations, respectively) of $CH{\equiv}H_4MPT^+$ and CH_3-H_4MPT concentrations. Combining reactions-4, 5 and 9 constrains the minimum value of pH_2 as:

$$\log pH_2 > \frac{1}{2}\left\{\log \frac{[CH_3\text{-H4 MPT}]}{[CH{\equiv}H4\ MPT^+]} - 3.9\right\} \quad (22)$$

Therefore, the allowed concentration range of $CH{\equiv}H_4$MPT and CH_3-H_4MPT of 100 M to 1 nM restricts the minimum pH_2 to 0.11 Pa for methanogenesis to proceed (i.e., all reactions except reaction-9 remain exergonic). This value is roughly consistent with the observation for marine sediments where methanogenesis appear to cease at ca. -10 kJ/mol (Hoehler et al., 2001) with a corresponding pH_2 of 0.25 Pa (with both CH_4 and CO_2 at 10^5 Pa).

While the above discussion provides thermodynamic constraints, low concentrations of CH_3-H_4MPT also limit MPR because the protein cost model takes into account the penalty for low metabolite concentrations with the reversible Michaelis-Menten kinetics term ($1+Km/C$) of the cost function (equation-2). The diffusion of metabolites from one enzyme to another, which is not considered in our model, may further limit the rate of methanogenesis because diffusive flux is proportional to the concentration gradient. If enzymes that catalyze the reaction-5 and reaction-6 (CH_3-H_4MPT:CH_3-CoM methyltransferase) are located in physical proximity (i.e., compartmentalized), the thermodynamic constraints can be relaxed by effectively combining reactions-5 and 6 (combined reaction can be exergonic while either reaction is endergonic). However, the enzyme catalyzing reaction-5 ($CH_2{=}H_4$MPT reductase) is cytoplasmic, while the enzyme for reaction-6 (CH_3-H_4MPT:CH_3-CoM methyltransferase) is membrane-bound, pointing against compartmentalization (e.g., Thauer et al., 2010). Understanding how methanogens cope with low concentrations of CH_3-H_4MPT is therefore important to consider for modeling methanogenesis under energy limited environments.

4.2 Isotopologue model explains experimental observations

Our model quantitatively explains carbon isotope systematics observed in laboratory culture experiments; the magnitude of carbon isotope fractionation increases as pH_2 decreases from 1 kPa to <10 Pa (Okumura et al., 2016; Topçuoğlu et al., 2019; Penning et al., 2005, Figure 5A). The model shows that the different magnitudes of observed carbon isotope fractionation

can be explained by increasing the reversibility of the first step of methanogenesis, the reduction of CO_2 to CHO-MFR.

Our model results also explain the effect of growth phase. Botz et al. (1993) reported that cultures under stationary phase produced larger carbon isotope fractionation (close to –80‰) than cultures under exponential growth phase. This growth phase effect can be explained, at least in part, by the dissolution rate limit because high cell density (>10^8 cells/mL) cultures during stationary phase would result in significant undersaturation of H_2 in a typical bioreactor set up (*see* equation-4). It is important to characterize k_La values for the experimental set up to evaluate the effect of pH_2, cell density, and growth phase on isotopologue fractionations.

At high pH_2 (pH_2 >1 kPa), D/H ratios of methane follow kinetic end-members, where the overall fractionation factor is the average of four primary D-KIEs (α_{ip}^+ values) of 0.659 (δD of -341‰). With assigned uncertainty of ±200‰ for KIEs (Table 6) for the first three primary D-KIEs, the solution (67 percentile) is -360±80‰ (the range is smaller than 200‰ by averaging effect). In comparison, laboratory cultures often produce a wider magnitude of D-KIE from -150 to -450‰ (Figure 5B). Some results can be explained by the effect of δD of H_2 (Kawagucci et al.,2014; Okumura et al., 2016). The δD values of H_2 can affect the δD of CH_4 (δD-H_2 effect) by D/H isotope exchange catalyzed by hydrogenases, production of metabolic water from H_2, and/or isoenzyme switching between H_2-forming and F_{420}-dependent methylene-H_4MPT (Burke, 1993; Kawagucci et al., 2014; Okumura et al., 2016). Significant deviation of δD values of intercellular water from environmental water is expected at high metabolic rates of laboratory cultures. These effects were important in culture experiments but less critical in nature, and not considered in our model. Okumura et al. (2016) noted that δD-H_2 effect is related to H_2 consumption rates, as slowly growing methanogens tend to show less δD-H_2 effect. This suggests that high δD-CH_4 values can also be related to cultures under the H_2 dissolution rate limit.

At low pH_2 between 10Pa and 1kPa, our model reproduced the relatively constant δD values of –300±40‰ for low pH_2 experiments ran as co-cultures (Figure 5B; Okumura et al.,2016). This is explained by the relatively high reversibility of reaction-5 that equilibrates the three methyl H atoms in CH_3-H_4MPT. The addition of the last H atom with D-KIE of ~0.4 explains the value of ca. –350±50‰ in the product CH_4 (Gruen et al., 2018). Considering the range of pH_2 in the environment, this solution explains the relatively constant D/H fractionations of 300±40‰ (e.g., Okumura et al., 2016; Waldron et al., 1999) between methane and water in natural settings. Such δD values have often been interpreted as the predominance of acetoclastic methanogenesis (e.g., Whiticar, 1999).

At high pH_2 (>1 kPa), the model solutions for $\Delta^{13}CH_3D$ range from -3.8 to +4.5‰, which is comparable to the range of $\Delta^{13}CH_3D$ values (–4.7 to 6.2‰) reported for laboratory cultures of hydrogenotrophic methanogens (Wang et al., 2015; Gruen et al., 2018; Stoler et al., 2015; Young et al., 2017) (Figure 5C). Our model suggests that a range of assigned γ_{cp}^+ values (0±8‰) explains all the culture data so far. Cao et al. (2019) proposed a simple formula for γ from reduced masses. However, the physical mechanism of clumped KIE is not well understood. The model predicts high $\Delta^{13}CH_3D$ values at intermediate pH_2 between 10 Pa and 1 kPa as a result of increased reversibility of reaction-5 (Figure 3; Figure 5C). The $\Delta^{13}CH_3D$ values of methane reach a minimum value at pH_2 <10 Pa because of the clumped KIE for C–H bond breaking process for reaction-7 (γ_{cp7}^- = 0.9923). $\Delta^{13}CH_3D$ values approach the equilibrium value only at very low pH_2 (<10 Pa), where methanogenesis may not proceed.

The values of $\Delta^{12}CH_2D_2$ reflect three effects: equilibrium, mixing and combinatorial effects. Mixing is non-linear for doubly-substituted isotopologues such that $\Delta^{12}CH_2D_2$ (and $\Delta^{13}CH_3D$) values of mixed methane is not a linear mixing of $\Delta^{12}CH_2D_2$ (and $\Delta^{13}CH_3D$) values of the two pools of methane being mixed (Young et al., 2016; Douglas et al., 2017; Defliese and Lohmann, 2015 for $^{47}CO_2$). The mixing relationship is quadratic to the mixing ratio (*f*) and the difference between the δD values of pools of CH species being mixed. For $\Delta^{13}CH_3D$ and $\Delta^{12}CH_2D_2$ the following approximations can be derived for mixing of two methane pools (A and B) (Supplementary material):

$$\Delta^{13}CD_{mix} \simeq (1-f)\Delta_A + f\,\Delta_B + f(1-f)\,(\delta^{13}C_A-\delta^{13}C_B)\,(\delta D_A-\delta D_B) \quad (23)$$

and

$$\Delta D_{2,\,mix} \simeq (1-f)\Delta_A + f\,\Delta_B + f(1-f)(\delta D_A-\delta D_B)^2 \quad (24)$$

where, *f* is the mixing ratio of pool B. For example, 1:1 mixing of CH-species that are different in δD by 300‰ yields 22.5‰ ($0.5 \times 0.5 \times 0.3^2 = 0.0225$) non-linearity in $\Delta^{12}CH_2D_2$ of the mixture. As the last square term is always positive for D_2 isotopologues, mixing of two pools of D_2 isotopologues produces positive bias. This mixing effect explains the relatively high $\Delta^{12}CH_2D_2$ values predicted for CH_2-H_4MPT, to CH_3-H_4MPT and CH_3-S-CoM under intermediate pH_2 (Figure 3-B).

Our model provides a framework to quantitatively describe the combinatorial effect that produces the highly negative $\Delta^{12}CH_2D_2$ values (-25 to -50‰ at pH_2>1kPa) observed for methanogen cultures (Young et al., 2017). The combinatorial effect is produced when two C–H bonds are formed sequentially, each of which derives from a distinct isotopic reservoir or is formed with a distinct KIE and ends up in symmetrically equivalent position in the product molecule. The magnitude of the combinatorial effect follows the ratio of geometric mean over arithmetic mean:

$$\Delta D_2 \simeq \left[\frac{\sqrt{\alpha_1\alpha_2}}{\frac{1}{2}(\alpha_1+\alpha_2)}\right]^2 - 1 \quad (25)$$

where α_1 and α_2 are KIEs for reactions forming the C–D bonds. Because the ratio of geometric over arithmetic means is always less than unity, combinatorial effects always produce negative ΔD_2 bias (Yeung, 2016; Röckmann et al., 2016). The model solutions for $\Delta^{12}CH_2D_2$ are asymmetric, and predict highly negative values (Figure 5D) when the range of α_{ip}^+ values (±0.2) are prescribed (Table 6).

Mechanistic understanding of the clumped isotopologue fractionation is still under development. Our isotopologue flow network model can provide a framework to understand the clumped isotopologue systematics once more experimental data under low pH_2 conditions become available.

4.3 Does near-equilibrium fractionation require anaerobic oxidation of methane?

Some studies attributed near-equilibrium isotopologue signals (i.e., δD ≃ –180‰, $\Delta^{13}CH_3D$ ≃ 5.7‰, $\Delta^{12}CH_2D_2$ ≃ 18.5‰) observed in nature to anaerobic oxidation of methane (AOM) (e.g., Ash et al.,2019; Giunta et al., 2019; 2021) because laboratory cultures of methanogens have exclusively produced methane with strong kinetic signals (Okumura et al., 2016; Valentine et al.,

2004; Gruen et al., 2018; Stolper et al.,2015; Young et al., 2017). While laboratory cultures performing AOM provide some indication of isotope equilibration, they did not produce equilibrium signals under the experimental conditions tested (Ono et al., 2021; Wegener et al., 2021). Although it is tempting to link near-equilibrium isotopologue signals to a specific microbial metabolism, such association is often asymmetrical. That is, while AOM likely produces near-equilibrium signals in CH_4, near-equilibrium signals may not necessarily be a result of AOM. Given the experimental conditions for most culture studies ($pH_2 > 10^5$ Pa), it is unclear if experimental studies can exclude the possibility that methanogenesis can produce near-equilibrium signals.

Sulfur isotope systems may offer a good historic example. It had been considered that larger than 46‰ KIE of $^{34}S/^{32}S$ between sulfate and sulfide indicates oxidative sulfur cycling and KIEs from sulfur disproportionation in addition to sulfate reduction (Canfield and Thamdrup, 1994). The threshold value of 46‰ was the maximum KIE produced by pure cultures of sulfate reducing microbes reported in Kaplan and Rittenberg (1964). After nearly five decades, the maximum value for pure cultures of sulfate reducing microbes was updated to 64‰ (Sim et al., 2011; Leavitt et al., 2013) demonstrating that sulfate reduction alone, under certain experimental (e.g., slow growth) conditions, can produce near-equilibrium sulfur isotope signals.

While experimental proof of methanogenic microbes producing near-equilibrium isotopologue signals may become available in the future, our study allows us to make predictions about isotopologue fractionations in natural settings. Our model suggests that it will be challenging to reproduce near-equilibrium signals by laboratory cultures of methanogens. This is because the production of near-equilibrium isotopologue signals requires conditions where the last step of methanogenesis (reaction-7) becomes (almost) fully reversible. Our model indicates that this occurs at $m H_2$ of less than 0.1 nM (saturation $pH_2 < 1$ Pa if equilibrium) (Figure 7). Methanogenesis does not occur or only proceeds at extremely slow rates below ca. 1 Pa because the *in vivo* concentration of CH_3-H_4MPT limits both the rate and thermodynamic limit of methanogenesis under low H_2 concentrations (section 4.1).

Most, if not all, enzymes that catalyze methanogenesis have been shown to be reversible (Scheller et al., 2010), and anaerobic methanotrophic archaea (ANME) performing AOM are thought to perform methanogenesis, or parts of the methanogenic metabolic pathway, in reverse (Thauer et al., 2011). Conversely, some studies hypothesized that ANME species, commonly found in symbiosis with sulfate reducers, are capable of both methanotrophy and methanogenesis. The evidence supporting this hypothesis includes abundant ANME genes in environments where net methanogenesis is occurring (Orcutt et al., 2005; Lloyd et al., 2011; Kevorkian et al., 2021), isotope studies of enrichment cultures (House et al., 2009; Bertram et al., 2013), and enrichment of ANME species under methanogenic conditions (Jagersma et al., 2012). Accordingly, commonly observed near-equilibrium methane isotopologue compositions below the sulfate-methane transition zone can be explained by ANME equilibrating methane isotopologues in deep subsurface sediments via slow methanogenesis.

What is required to produce equilibrium isotopologue signals can be reduced to the enzyme catalyzing reaction-7, methyl-coenzyme M reductase (MCR). The rate of equilibration can be estimated from the concentrations of MCR in sediments. Both methanogens and ANME carry MCR although it is more abundant in ANME (Hallman et al., 2004; Heller et al., 2008). Scheller et al. (2010) reported that MCR purified from methanogens (*M. marburgensis*) catalyzes methane oxidation at 11.4 nmol min^{-1} mg-MCR^{-1} at 1 mM CH_4 (k_{cat} = 53 s^{-1}). Inagaki et al. (2015)

reported F_{430} concentrations from 0.2 to 60 fmol/g of sediments for deep sea sediments from 100 to 2000 m below the seafloor. Since one mole of MCR contains 2 moles of F_{430} cofactor (Ellefson et al., 1982), this translates to MCR concentrations of 0.1 to 30 fmol/g sediments, and a methane turnover rate of 530 fmol s^{-1} g-$sediment^{-1}$ is derived (k_{cat} times MCR concentration of 10 fmol/g sediments). Assuming a porosity of 50% and CH_4 concentration of 10 mM in porewater gives 5 µmol of CH_4 per gram of deep sediments and methane turnover time of 0.3 years. The actual rate of equilibration may be slower because reaction-7 requires cofactors (HS-CoB and CoM-S-S-CoB; Table 1). The exchange rate might also be limited by the diffusion of substrates in the sediment. Nevertheless, the exchange timescale of less than a year is much shorter compared to the timescale of sedimentation (millions of years per km) and slow metabolisms of the deep biosphere (turn over time as slow as 100 years, e.g., Trembath-Reinchert, 2017). Therefore, near-equilibrium methane isotopologue signals can be reasonably expected for deep sediments that carry intact MCRs but not necessarily indicate the process of AOM. The MCR could be from ANME or nominally methanogenic microbes, and the equilibration process can be linked to the net methanogenesis or methanotrophy. Our model can be applied to model AOM to explore its isotopologue systematics in the future to test the hypothesis.

5 Conclusions

The pathway protein cost and isotopologue flow network models were applied to quantitatively describe $^{13}C/^{12}C$, D/H, $^{13}CH_3D$, and $^{12}CH_2D_2$ fractionations during hydrogenotrophic methanogenesis. Based on the thermodynamics and kinetic data for enzymatic reactions, the model predicts reversibilities of 8 reactions for methanogenesis pathway. The isotopologue ratios of methane and all intermediate metabolites are solved as a function of reversibilities and prescribed fractionation factors. The model can explain a number of observations for laboratory culture experiments, including the range of $^{13}C/^{12}C$ fractionation of 40 to 80‰ between CH_4 and CO_2 as a function of pH_2, and relatively constant kinetic D/H fractionations of 300±40‰ between methane and water. The model also can make accurate predictions for doubly substituted isotopologues, $^{13}CH_3D$ and $^{12}CH_2D_2$. The pathway thermodynamics and isotopologue flow network model scheme presented herein can be applied and expanded to predict isotope and isotopologue fractionations for a range of metabolisms.

Acknowledgements: We thank the associate editor (Ed Hornibrook) and two anonymous reviewers for constructive comments. This work was supported by the NASA Astrobiology Institute "Rock-Powered Life" project under cooperative agreement NNA15BB02A, NSF-Geobiology and Low Temperature Geochemistry, EAR-1852946, N. Braunsdorf and D. Smit of Shell PTI/EG, and the Deep Carbon Observatory (to S.O.). J.H.R. was also supported by the Grayce B. Kerr Fellowship, the Robert R. Shrock Fellowship, and the Callahan Dee Fellowship at MIT.

References

Ash J. L., Egger M., Treude T., Kohl I., Cragg B., Parkes R. J., Slomp C. P., Lollar B. S. and Young E. D. (2019) Exchange catalysis during anaerobic methanotrophy revealed by $^{12}CH_2D_2$ and $^{13}CH_3D$ in methane. *Geochemical Perspect. Lett.* **10**, 26–30.

766 Balabane, M., Galimov, E., Hermann, M., Létolle, R. (1987) Hydrogen and carbon isotope
767 fractionation during experimental production of bacterial methane. *Organic Geochemistry*
768 **11**, 115–119.
769 Belyaev, S.S., Wolkin, R., Kenealy, W.R., DeNiro, M.J., Epstein, S., Zeikus, J.G. (1983)
770 Methanogenic Bacteria from the Bondyuzhskoe Oil Field: General Characterization and
771 Analysis of Stable-Carbon Isotopic Fractionation. *Appl Environ Microbiol* **45**, 691–697.
772 Bell R. P. (1973) Kinetic Isotope Effects in Proton-Transfer Reactions. In *The Proton in Chemistry*
773 Springer US, Boston, MA. pp. 250–296.
774 Bertram S., Blumenberg M., Michaelis W., Siegert M., Krüger M. and Seifert R. (2013)
775 Methanogenic capabilities of ANME-archaea deduced from ^{13}C-labelling approaches.
776 *Environ. Microbiol.* **15**, 2384–2393.
777 Bigeleisen J. (1949) The relative reaction velocities of isotopic molecules. *J. Chem. Phys.* **17**, 675–
778 678.
779 Bigeleisen J. (1955) Statistical mechanics of isotopic systems with small quantum corrections. I.
780 general considerations and the rule of the geometric mean. *J. Chem. Phys.* **23**, 2264–2267.
781 Boone D. R., Johnson R. L. and Liu Y. (1989) Diffusion of the interspecies electron carriers H2 and
782 formate in methanogenic ecosystems and its implications in the measurement of Km for
783 H_2 or formate uptake. *Appl. Environ. Microbiol.* **55**, 1735–1741.
784 Botz R., Pokojski H. D., Schmitt M. and Thomm M. (1997) Carbon isotope fractionation during
785 bacterial methanogenesis by CO_2 reduction. *Org. Geochem.* **25**, 255–262.
786 Brunner B. and Bernasconi S. M. (2005) A revised isotope fractionation model for dissimilatory
787 sulfate reduction in sulfate reducing bacteria. *Geochim. Cosmochim. Acta* **69**, 4759–4771.
788 Burke A. R. (1993) Possible Influence of hydrogen concentration on microbial methane stable
789 hydrogen isotopic composition. *Chemosphere* **26**, 55–67.
790 Canfield D. E. and Thamdrup B. (1994) The production of ^{34}S-depleted sulfide during bacterial
791 disproportionation of elemental sulfur. *Science* **266**, 1973–1975.
792 Cao X., Bao H. and Peng Y. (2019) A kinetic model for isotopologue signatures of methane
793 generated by biotic and abiotic CO2 methanation. *Geochim. Cosmochim. Acta* **249**, 59–75.
794 Cha Y., Murray C. J. and Klinman J. P. (1989) Hydrogen tunneling in enzyme reactions. *Science*
795 **243**, 1325–1330.
796 Cord-Ruwisch R., Seitz H. J. and Conrad R. (1988) The capacity of hydrogenotrophic anaerobic
797 bacteria to compete for traces of hydrogen depends on the redox potential of the terminal
798 electron acceptor. *Arch. Microbiol.* **149**, 350–357.
799 Costa K. C., Yoon S. H., Pan M., Burn J. A., Baliga N. S. and Leigh J. A. (2013) Effects of H2 and
800 formate on growth yield and regulation of methanogenesis in *Methanococcus maripaludis*.
801 *J. Bacteriol.* **195**, 1456–1462.
802 Daniels L. (1993) Biochemistry of methanogenesis. In *New Comprehensive Biochemistry. Elsevier*
803 pp. 41–112.
804 Defliese W. F. and Lohmann K. C. (2015) Non-linear mixing effects on mass-47 CO2 clumped
805 isotope thermometry: Patterns and implications. *Rapid Commun. Mass Spectrom.* **29**, 901–
806 909.
807 Douglas P. M. J., Stolper D. A., Eiler J. M., Sessions A. L., Lawson M., Shuai Y., Bishop A., Podlaha
808 O. G., Ferreira A. A., Santos Neto E. V., Niemann M., Steen A. S., Huang L., Chimiak L.,
809 Valentine D. L., Fiebig J., Luhmann A. J., Seyfried W. E., Etiope G., Schoell M., Inskeep W. P.,

Moran J. J. and Kitchen N. (2017) Methane clumped isotopes: progress and potential for a new isotopic tracer. *Org. Geochem.* **113**, 262–282.

Farquhar J., Johnston D. T., Wing B. A., Habicht K. S., Canfield D. E., Airieau S. and Thiemens M. H. (2003) Multiple sulphur isotopic interpretations of biosynthetic pathways: implications for biological signatures in the sulphur isotope record. *Geobiology* **1**, 27–36.

Ferry J. G. (1993) *Methanogenesis*. ed. J. G. Ferry, Springer US, Boston, MA.

Flamholz A., Noor E., Bar-Even A., Liebermeister W. and Milo R. (2013) Glycolytic strategy as a tradeoff between energy yield and protein cost. *Proc. Natl. Acad. Sci. U. S. A.* **110**, 10039–10044.

Games, L.M., HayesRobert, J.M., Gunsalus, P. (1978) Methane-producing bacteria: natural fractionations of the stable carbon isotopes. *Geochimica et Cosmochimica Acta* **42**, 1295–1297.

Garcia-Ochoa F. and Gomez E. (2005) Prediction of gas-liquid mass transfer coefficient in sparged stirred tank bioreactors. *Biotechnol. Bioeng.* **92**, 761–772.

Giunta T., Labidi J., Kohl I. E., Ruffine L., Donval J. P., Géli L., Çağatay M. N., Lu H. and Young E. D. (2021) Evidence for methane isotopic bond re-ordering in gas reservoirs sourcing cold seeps from the Sea of Marmara. *Earth Planet. Sci. Lett.* **553**.

Giunta T., Young E. D., Warr O., Kohl I., Ash J. L., Martini A., Mundle S. O. C., Rumble D., Pérez-Rodríguez I., Wasley M., LaRowe D. E., Gilbert A. and Sherwood Lollar B. (2019) Methane sources and sinks in continental sedimentary systems: New insights from paired clumped isotopologues $^{13}CH_3D$ and $^{12}CH_2D_2$. *Geochim. Cosmochim. Acta* **245**, 327–351.

Goldman M. J., Vandewiele N. M., Ono S. and Green W. H. (2019) Computer-generated isotope model achieves experimental accuracy of filiation for position-specific isotope analysis. *Chem. Geol.* **514**, 1–9.

Gropp J., Iron M. A. and Halevy I. (2021) Theoretical estimates of equilibrium carbon and hydrogen isotope effects in microbial methane production and anaerobic oxidation of methane. *Geochim. Cosmochim. Acta* **295**, 237–264.

Gruen D. S., Wang D. T., Könneke M., Topçuoğlu B. D., Stewart L. C., Goldhammer T., Holden J. F., Hinrichs K.-U. and Ono S. (2018) Experimental investigation on the controls of clumped isotopologue and hydrogen isotope ratios in microbial methane. *Geochim. Cosmochim. Acta* **237**, 339–356.

Hallam S. J., Girguis P. R., Preston C. M., Richardson P. M. and DeLong E. F. (2003) Identification of methyl coenzyme M reductase A (mcrA) genes associated with methane-oxidizing archaea. *Appl. Environ. Microbiol.* **69**, 5483–5491.

Hayes J. M. (2019) Fractionation of carbon and hydrogen isotopes in biosynthetic processes. In *Stable Isotope Geochemistry* pp. 225–277.

Heller C., Hoppert M. and Reitner J. (2008) Immunological localization of coenzyme M reductase in anaerobic methane-oxidizing archaea of ANME 1 and ANME 2 type. *Geomicrobiol. J.* **25**, 149–156.

Hendrickson, E. L., A. K. Haydock, B. C. Moore, W. B. Whitman, and J. A. Leigh (2007) Functionally distinct genes regulated by hydrogen limitation and growth rate in methanogenic archaea. *Proc Natl Acad Sci.* **104**, 8930-8934.

Hermes J. D., Morrical S. W., O'Leary M. H. and Cleland W. W. (1984) Variation of Transition-State Structure as a Function of the Nucleotide in Reactions Catalyzed by Dehydrogenases. 2. Formate Dehydrogenase. *Biochemistry* **23**, 5479–5488.

Hoehler T. M. (2004) Biological energy requirements as quantitative boundary conditions for life in the subsurface. *Geobiology* **2**, 205–215.

Hoehler T. M., Alperin M. J., Albert D. B. and Martens C. S. (2001) Apparent minimum free energy requirements for methanogenic Archaea and sulfate-reducing bacteria in an anoxic marine sediment. *FEMS Microbiol. Ecol.* **38**, 33–41.

Horibe, Y., Craig, H. (1995) D/H fractionation in the system methane-hydrogen-water. *Geochimica et Cosmochimica Acta* **59**, 5209–5217.

Horita, J. (2001) Carbon isotope exchange in the system CO_2-CH_4 at elevated temperatures. *Geochimica et Cosmochimica Acta* **65**, 1907–1919.

House C. H., Orphan V. J., Turk K. A., Thomas B., Pernthaler A., Vrentas J. M. and Joye S. B. (2009) Extensive carbon isotopic heterogeneity among methane seep microbiota. *Environ. Microbiol.* **11**, 2207–2215.

Jagersma C. G., Meulepas R. J. W., Timmers P. H. A., Szperl A., Lens P. N. L. and Stams A. J. M. (2012) Enrichment of ANME-1 from Eckernförde Bay sediment on thiosulfate, methane and short-chain fatty acids. *J. Biotechnol.* **157**, 482–489.

Jautzy, J. J., Douglas, P. M. J., Xie, H., Eiler, J. M., & Clark, I. D. (2021). CH_4 isotopic ordering records ultra-slow hydrocarbon biodegradation in the deep subsurface. *Earth and Planetary Science Letters*, **562**, 116841.

Jud G., Schneider K. and Bachofen R. (1997) The role of hydrogen mass transfer for the growth kinetics of Methanobacterium thermoautotrophicum in batch and chemostat cultures. *J. Ind. Microbiol. Biotechnol.* **19**, 246–251.

Kawagucci S., Kobayashi M., Hattori S., Yamada K., Ueno Y., Takai K. and Yoshida N. (2014) Hydrogen isotope systematics among H2-H2O-CH4 during the growth of the hydrogenotrophic methanogen Methanothermobacter thermautotrophicus strain δH. *Geochim. Cosmochim. Acta* **142**, 601–614.

Kevorkian R. T., Callahan S., Winstead R. and Lloyd K. G. (2021) ANME-1 archaea may drive methane accumulation and removal in estuarine sediments. *Environ. Microbiol. Rep.* **13**, 185–194.

Klein A. R. and Thauer R. K. (1995) Re-Face Specificity at C14a of Methylenetetrahydromethanopterin and Si-Face Specificity at C5 of Coenzyme F_{420} for Coenzyme F_{420}-Dependent Methylenetetrahydromethanopterin Dehydrogenase from Methanogenic Archaea. *Eur. J. Biochem.* **227**, 169–174.

Kueter N., Schmidt M. W., Lilley M. D. and Bernasconi S. M. (2019) Experimental determination of equilibrium CH_4-CO_2-CO carbon isotope fractionation factors (300-1200 C). *Earth Planet. Sci. Lett.* **506**, 64-75.

Krzycki, J.A., Kenealy, W.R., DeNiro, M.J., Zeikus, J.G. (1987) Stable Carbon Isotope Fractionation by *Methanosarcina barkeri* during Methanogenesis from Acetate, Methanol, or Carbon Dioxide-Hydrogen. *Appl Environ Microbiol* **53**, 2597–2599.

Leavitt W. D., Halevy I., Bradley A. S. and Johnston D. T. (2013) Influence of sulfate reduction rates on the Phanerozoic sulfur isotope record. *Proc. Natl. Acad. Sci. U. S. A.* **110**, 11244–11249.

Livingston D. J., Fox J. A., Orme-Johnson W. H. and Walsh C. T. (1987) 8-Hydroxy-5-deazaflavin-reducing hydrogenase from Methanobacterium thermoautotrophicum: 2. Kinetic and hydrogen-transfer studies. *Biochemistry* **26**, 4228–37.

Lloyd K. G., Alperin M. J. and Teske A. (2011) Environmental evidence for net methane production and oxidation in putative ANaerobic MEthanotrophic (ANME) archaea. *Environ. Microbiol.* **13**, 2548–2564.

Meister, P., Liu, B., Khalili, A., Böttcher, M.E., Jørgensen, B.B. (2019) Factors controlling the carbon isotope composition of dissolved inorganic carbon and methane in marine porewater: An evaluation by reaction-transport modelling. *Journal of Marine Systems,* **200**, 103227.

Miller, H. M., Chaudhry, N., Conrad, M. E., Bill, M., Kopf, S. H., & Templeton, A. S. (2018). Large carbon isotope variability during methanogenesis under alkaline conditions. *Geochimica et Cosmochimica Acta*, **237**, 18–31.

Morgan, R. M., T. D. Pihl, J. Nölling, and J. N. Reeve (1997) Hydrogen regulation of growth, growth yields, and methane gene transcription in Methanobacterium thermoautotrophicum. *J. Bacteriol*. **179**, 889–898.

Müller A. L., Gu W., Patsalo V., Deutzmann J. S., Williamson J. R. and Spormann A. M. (2021) An alternative resource allocation strategy in the chemolithoautotrophic archaeon Methanococcus maripaludis . *Proc. Natl. Acad. Sci.* **118**, e2025854118.

Nölling, J., T. D. Pihl, A. Vriesema, and J. N. Reeve (1995) Organization and growth phase-dependent transcription of methane genes in two regions of the Methanobacterium thermoautotrophicum genome. *J. Bacteriol*. **177**, 2460–2468.

Noor E., Bar-Even A., Flamholz A., Reznik E., Liebermeister W. and Milo R. (2014) Pathway Thermodynamics Highlights Kinetic Obstacles in Central Metabolism. *PLoS Comput. Biol.* **10**.

Okumura T., Kawagucci S., Saito Y., Matsui Y., Takai K. and Imachi H. (2016) Hydrogen and carbon isotope systematics in hydrogenotrophic methanogenesis under H2-limited and H2-enriched conditions: implications for the origin of methane and its isotopic diagnosis. *Prog. Earth Planet. Sci.* **3**, 2–15.

Ono S., Rhim J. H., Gruen D. S., Taubner H., Kölling M. and Wegener G. (2021) Clumped isotopologue fractionation by microbial cultures performing the anaerobic oxidation of methane. *Geochim. Cosmochim. Acta* **293**, 70–85.

Ono, S., Rhim, J. H., Gruen, D. S., Taubner, H., Kölling, M., & Wegener, G. (2021). Clumped isotopologue fractionation by microbial cultures performing the anaerobic oxidation of methane. *Geochimica et Cosmochimica Acta*, **293**, 70–85.

Orcutt B., Boetius A., Elvert M., Samarkin V. and Joye S. B. (2005) Molecular biogeochemistry of sulfate reduction, methanogenesis and the anaerobic oxidation of methane at Gulf of Mexico cold seeps. *Geochim. Cosmochim. Acta* **69**, 4267–4281.

Pauss A., Andre G., Perrier M. and Guiot S. R. (1990) Liquid-to-Gas Mass Transfer in Anaerobic Processes: Inevitable Transfer Limitations of Methane and Hydrogen in the Biomethanation Process. *Appl. Environ. Microbiol.* **56**, 1636–44.

Penning H., Plugge C. M., Galand P. E. and Conrad R. (2005) Variation of carbon isotope fractionation in hydrogenotrophic methanogenic microbial cultures and environmental samples at different energy status. *Glob. Chang. Biol.* **11**, 2103–2113.

Peterson J. R., Labhsetwar P., Ellermeier J. R., Kohler P. R. A., Jain A., Ha T., Metcalf W. W. and Luthey-Schulten Z. (2014) Towards a computational model of a methane producing archaeum. *Archaea* **2014**.

Rees C. E. (1973) A steady-state model for sulphur isotope fractionation in bacterial reduction processes. *Geochim. Cosmochim. Acta* **37**, 1141–1162.

Röckmann T., Popa M. E., Krol M. C. and Hofmann M. E. G. (2016) Statistical clumped isotope signatures. *Sci. Rep.* **6**.

Roston D. and Kohen A. (2010) Elusive transition state of alcohol dehydrogenase unveiled. *Proc. Natl. Acad. Sci. U. S. A.* **107**, 9572–9577.

Rucker J. and Klinman J. P. (1999) Computational study of tunneling and coupled motion in alcohol dehydrogenase-catalyzed reactions: Implication for measured hydrogen and carbon isotope effects. *J. Am. Chem. Soc.* **121**, 1997–2006.

Scharschmidt M., Fisher M. A. and Cleland W. W. (1984) Variation of Transition-State Structure as a Function of the Nucleotide in Reactions Catalyzed by Dehydrogenases. 1. Liver Alcohol Dehydrogenase with Benzyl Alcohol and Yeast Aldehyde Dehydrogenase with Benzaldehyde†. *Biochemistry* **23**, 5471–5478.

Scheller S., Goenrich M., Boecher R., Thauer R. K. and Jaun B. (2010) The key nickel enzyme of methanogenesis catalyses the anaerobic oxidation of methane. *Nature* **465**, 606–608.

Scheller S., Goenrich M., Thauer R. K. and Jaun B. (2013) Methyl-coenzyme M reductase from methanogenic archaea: Isotope effects on the formation and anaerobic oxidation of methane. *J. Am. Chem. Soc.* **135**, 14975–14984.

Sim M. S., Bosak T. and Ono S. (2011) Large sulfur isotope fractionation does not require disproportionation. *Science* **333**, 74–77.

Stolper, D. A., Lawson, M., Davis, C. L., Ferreira, A. A., Santos Neto, E. v., Ellis, G. S., Lewan, M. D., Martini, A. M., Tang, Y., Schoell, M., Sessions, A. L., & Eiler, J. M. (2014). Formation temperatures of thermogenic and biogenic methane. *Science* **344**, 1500–1503.

Stolper D. A., Martini A. M., Clog M., Douglas P. M., Shusta S. S., Valentine D. L., Sessions A. L. and Eiler J. M. (2015) Distinguishing and understanding thermogenic and biogenic sources of methane using multiply substituted isotopologues. *Geochim. Cosmochim. Acta* **161**, 219–247.

Thauer R. K., Kaster A. K., Seedorf H., Buckel W. and Hedderich R. (2008) Methanogenic archaea: Ecologically relevant differences in energy conservation. *Nat. Rev. Microbiol.* **6**, 579–591.

Thauer R. K., Kaster A.-K., Goenrich M., Schick M., Hiromoto T. and Shima S. (2010) Hydrogenases from Methanogenic Archaea, Nickel, a Novel Cofactor, and H_2 Storage. *Annu. Rev. Biochem.* **79**, 507–536.

Topçuoğlu B. D., Meydan C., Nguyen T. B., Lang S. Q. and Holden J. F. (2019) Growth kinetics, carbon isotope fractionation, and gene expression in the hyperthermophile Methanocaldococcus jannaschii during hydrogen-limited growth and interspecies hydrogen transfer. *Appl. Environ. Microbiol.* **85**, 1–14.

Trembath-Reichert E., Morono Y., Ijiri A., Hoshino T., Dawson K. S., Inagaki F. and Orphan V. J. (2017) Methyl-compound use and slow growth characterize microbial life in 2-km-deep subseafloor coal and shale beds. *Proc. Natl. Acad. Sci. U. S. A.* **114**, E9206–E9215.

Turner, A. C., Korol, R., Eldridge, D. L., Bill, M., Conrad, M. E., Miller, T. F., & Stolper, D. A. (2021). Experimental and theoretical determinations of hydrogen isotopic equilibrium in the system CH_4-H_2-H_2O from 3 to 200 °C. *Geochimica et Cosmochimica Acta*. **314**, 223-269

Valentine D. L., Blanton D. C. and Reeburgh W. S. (2000) Hydrogen production by methanogens under low-hydrogen conditions. *Arch. Microbiol.* **174**, 415–421.

Valentine D. L., Reeburgh W. S. and Blanton D. C. (2000) A culture apparatus for maintaining H2 at sub-nanomolar concentrations. *J. Microbiol. Methods* **39**, 243–251.

Waldron S., Lansdown J. M., Scott E. M., Fallick A. E. and Hall A. J. (1999) The global influence of the hydrogen isotope composition of water on that of bacteriogenic methane from shallow freshwater environments. *Geochim. Cosmochim. Acta* **63**, 2237–2245.

Wang D. T., Gruen D. S., Sherwood Lollar B., Hinrichs K.-U., Stewart L. C., Holden J. F., Hristov A. N., Pohlman J. W., Morrill P. L., Könneke M., Delwiche K. B., Reeves E. P., Sutcliffe C. N., Ritter D. J., Seewald J. S., McIntosh J. C., Hemond H. F., Kubo M. D., Cardace D., Hoehler T. M. and Ono S. (2015) Nonequilibrium clumped isotope signals in microbial methane. *Science* **348**.

Warr, O., Young, E.D., Giunta, T., Kohl, I.E., Ash, J.L., Lollar, B.S. (2021) High-resolution, long-term isotopic and isotopologue variation identifies the sources and sinks of methane in a deep subsurface carbon cycle. *Geochimica et Cosmochimica Acta* **294**, 315–334.

Wegener G., Gropp J., Taubner H., Halevy I. and Elvert M. (2021) Sulfate-dependent reversibility of intracellular reactions explains the opposing isotope effects in the anaerobic oxidation of methane. *Sci. Adv.* **7**, 1–14.

Whitehill A. R., Joelsson L. M. T., Schmidt J. A., Wang D. T., Johnson M. S. and Ono S. (2017) Clumped isotope effects during OH and Cl oxidation of methane. *Geochim. Cosmochim. Acta* **196**, 307–325.

Whiticar M. J. (1999) Carbon and hydrogen isotope systematics of bacterial formation and oxidation of methane. *Chem. Geol.* **161**, 291–314.

Whiticar, M. J., Faber, E., & Schoell, M. (1986). Biogenic methane formation in marine and freshwater environments: CO_2 reduction vs. acetate fermentation—Isotope evidence. *Geochimica et Cosmochimica Acta*, **50**, 693–709.

Wing B. A. and Halevy I. (2014) Intracellular metabolite levels shape sulfur isotope fractionation during microbial sulfate respiration. *Proc. Natl. Acad. Sci. U. S. A.* **111**, 18116–18125.

Yeung L. Y. (2016) Combinatorial effects on clumped isotopes and their significance in biogeochemistry. *Geochim. Cosmochim. Acta* **172**, 22–38.

Young E. D., Kohl I. E., Lollar B. S., Etiope G., Rumble D., Li (李姝宁) S., Haghnegahdar M. A., Schauble E. A., McCain K. A., Foustoukos D. I., Sutclife C., Warr O., Ballentine C. J., Onstott T. C., Hosgormez H., Neubeck A., Marques J. M., Pérez-Rodríguez I., Rowe A. R., LaRowe D. E., Magnabosco C., Yeung L. Y., Ash J. L. and Bryndzia L. T. (2017) The relative abundances of resolved $^{l2}CH_2D_2$ and $^{13}CH_3D$ and mechanisms controlling isotopic bond ordering in abiotic and biotic methane gases. *Geochim. Cosmochim. Acta* **203**, 235–264.

Yoshioka, H., Sakata, S., Kamagata, Y., (2008) Hydrogen isotope fractionation by Methanothermobacter thermoautotrophicus in coculture and pure culture conditions. *Geochimica et Cosmochimica Acta* **72**, 2687–2694.

Zinder S. H. (1993) Physiological Ecology of Methanogens. In Methanogenesis Springer US, Boston, MA. pp. 128–206.

1024 Zirngibl C., Dongen W., Schworer B., Bunau R., Richter M., Klein A., & Thauer R.K. (1992) H2-
1025 forming methylenetetrahydromethanopterin dehydrogenase, a novel type of hydrogenase
1026 without iron-sulfur clusters in methanogenic archaea. European Journal of Biochemistry 208,
1027 511–520.
1028

Figures

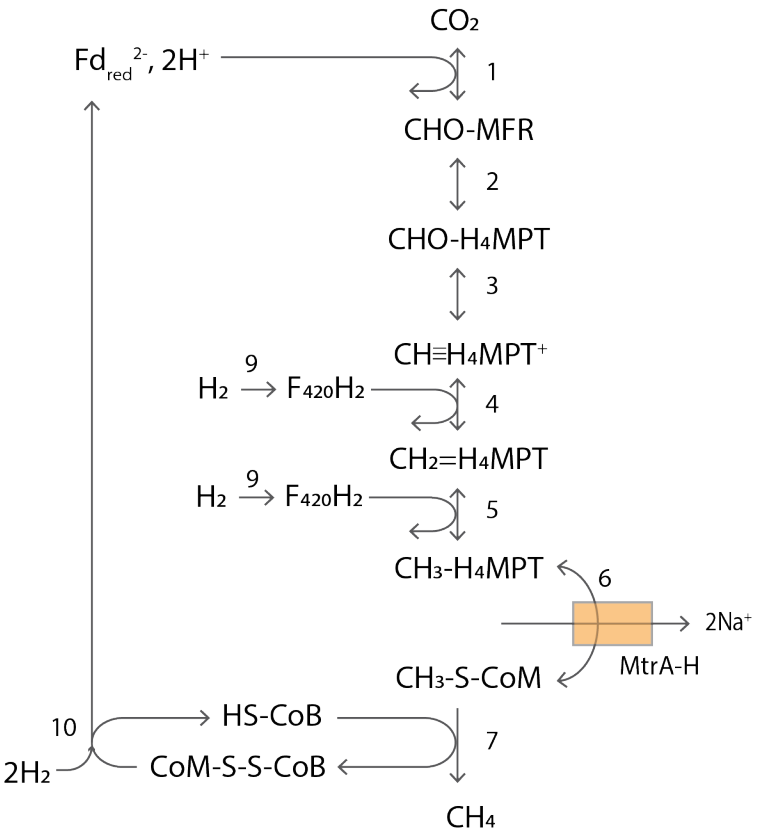

Figure 1: Pathway for hydrogenotrophic methanogens without cytochromes based on Thauer et al. (2008). Reactions and abbreviations for cofactors are listed in Table 1. Numbers by the arrows correspond to the reaction numbers in Table 1. Reaction-6 is coupled with Na^+ translocation by enzyme MtrA-H.

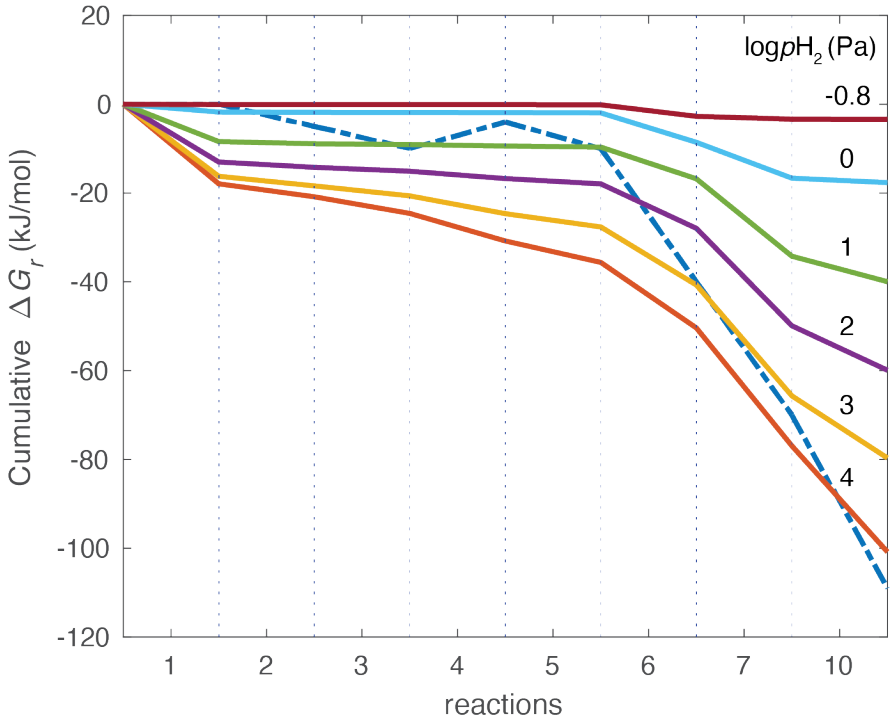

Figure 2: Pathway protein cost model results for cumulative free energy yields for methanogenic reactions under 10^4 to $10^{-0.8}$ Pa pH_2 (solid lines). Dashed line corresponds to free energy yields at standard conditions (i.e., concentrations at 1 M for dissolved and 1 bar for gaseous species at 25 °C and pH 7). Reactions are listed in Table 1. Methanogenesis (equation-1) yields –131 kJ/mol at standard conditions. The diagram shows –109 kJ/mol at the standard condition because reaction-8 and 9 are reactions for co-factors and not included in the protein cost model.

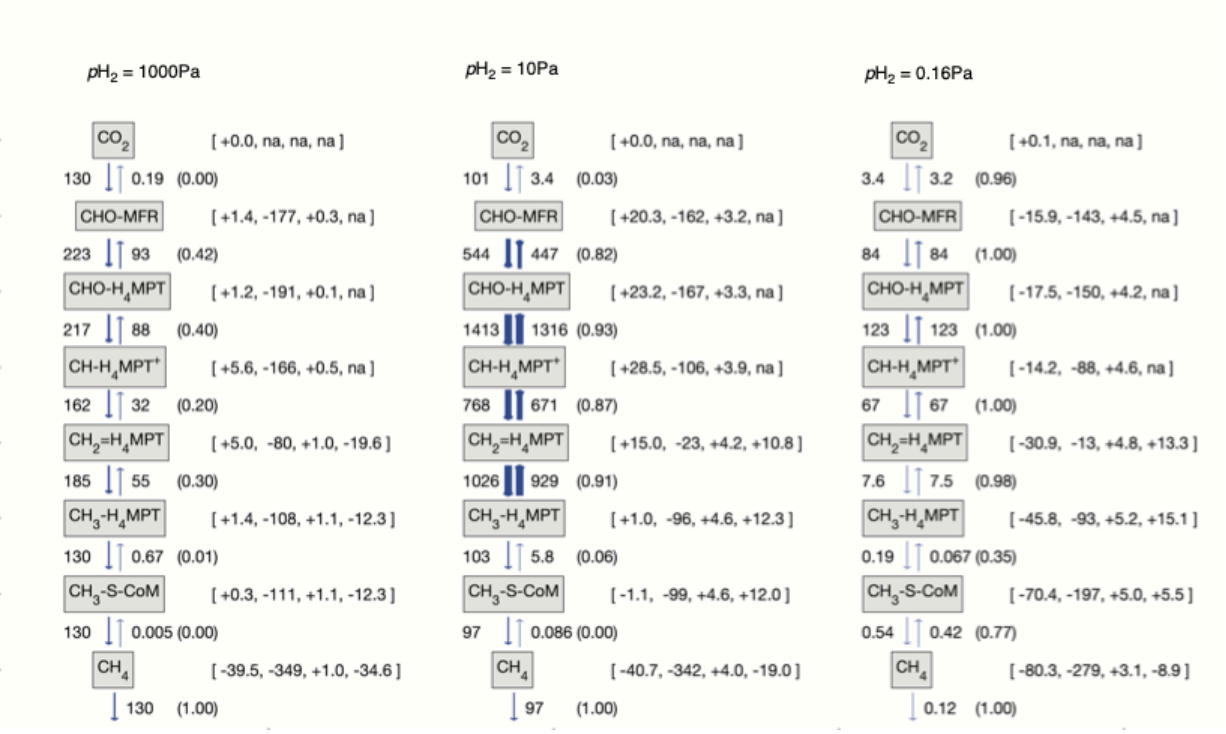

Figure 3: Pathway fluxes and isotopologue compositions for metabolites involved in hydrogenotrophic methanogenesis at three pH_2 conditions. Pathway fluxes are in mmol g-protein^{-1} hour^{-1}, reversibility are shown in round brackets, and isotopologue compositions (in ‰) are listed in square brackets as [$\delta^{13}C$, δD, $\Delta^{13}CD$, and ΔD_2]. The isotope ratios are normalized by $\delta^{13}C\text{-}CO_{2(gas)}$ and $\delta D\text{-}H_2O_{(l)}$ as 0 ‰. Thickness of the arrows corresponds (by a non-linear function) to the relative size of fluxes. The model solution does not change significantly at pH_2 above 1000Pa.

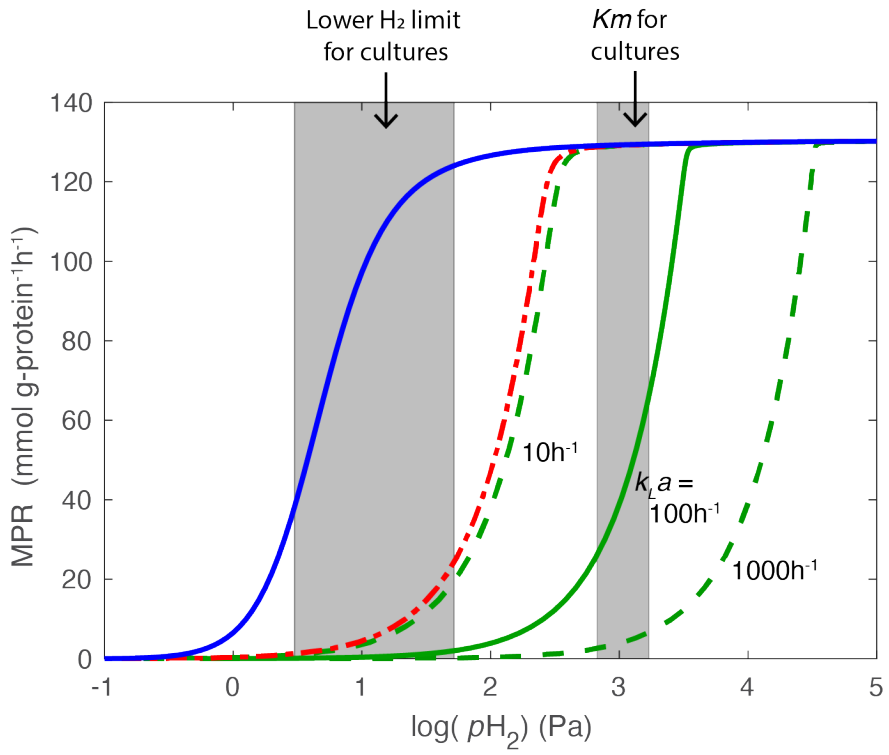

Figure 4: Methane production rate (MPR) as a function of pH2 predicted by the protein cost model. Blue line shows the model result without transport limits, red and green lines are the results including diffusion (equation-4) and dissolution (equation-6) limits, respectively. The observed ranges for apparent half saturation constant (K_m) and lower H_2 limit of methanogenesis for batch cultures are also shown in grey shaded areas (Cord-Ruswisch et al., 1988; Zinder, 1993).

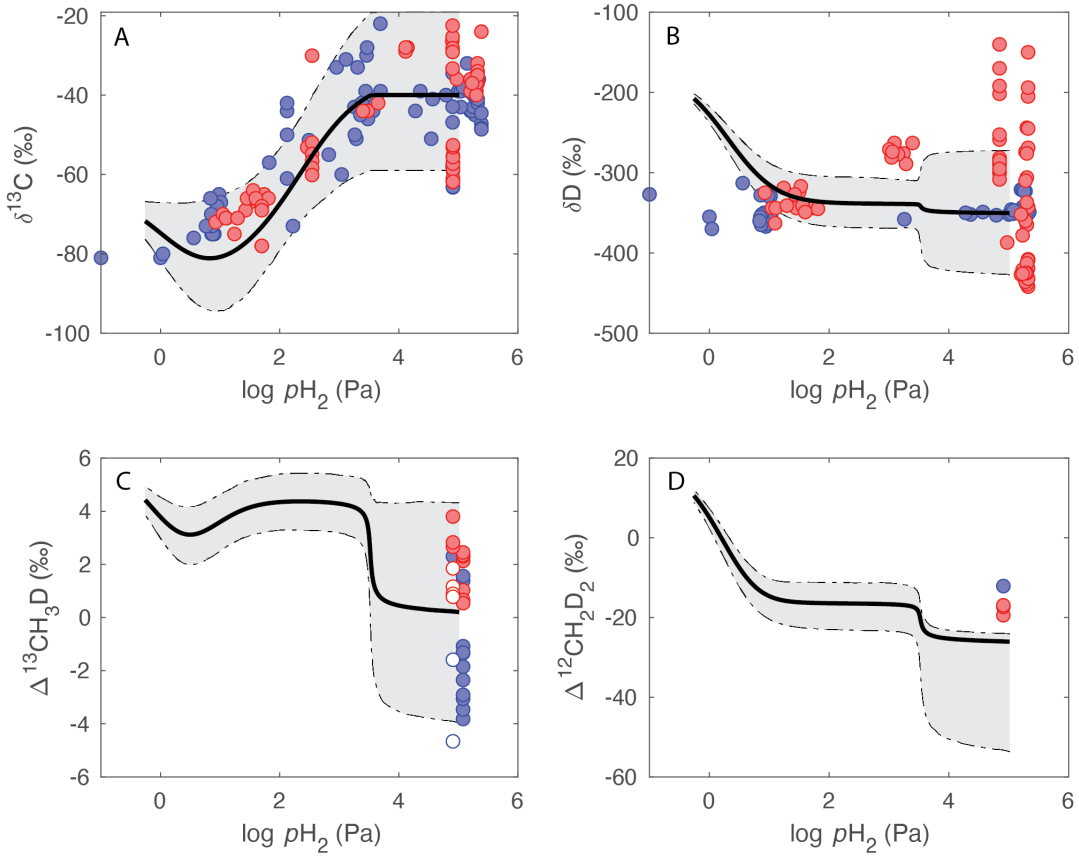

Figure 5: Results of isotopologue flow network model showing the isotope and isotopologue compositions of the final product CH_4. The model was run with k_La = 100 h^{-1} and cell density of 10^7 cells/mL. The solid line shows the model with default values of fractionation factors. The grey area shows the results of Monte Calro simulation (n=1000, 67 percentile) using a range of fractionation factors shown in Table 6. Data from laboratory cultures are also plotted for thermophilic (red circles) and mesophilic methanogens (blue circles). Data source for culture studies are Okumura et al., (2016), Penning et al. (2005), Topçuoğlu et al., (2019), Valentine et al. (2004), Games et al. (1978), Belyaev et al.(1983), Krzycki et al. (1987), Balabane et al. (1987), Botz et al. (1996), Yoshioka et al. (2008) for $\delta^{13}C$ and δD, and Gruen et al. (2018), Stolper et al. (2015), Giunta et al. (2021), and Young et al. (2017) for $\Delta^{13}CH_3D$ and $\Delta^{12}CH_2D_2$. Botz et al. (1996) reported relatively small ^{13}C-fractionations during log-phase growth; these data were excluded in the plot. Stolper et al. (2015) reported Δ_{18} values (combined $^{13}CH_3D$ and $^{12}CH_2D_2$); their values are shown in open red and blue circles for thermophilic and mesophilic methanogens, respectively. These Δ_{18} values can be different from $\Delta^{13}CH_3D$ by up to 0.5‰ depending upon their $\Delta^{12}CH_2D_2$ values.

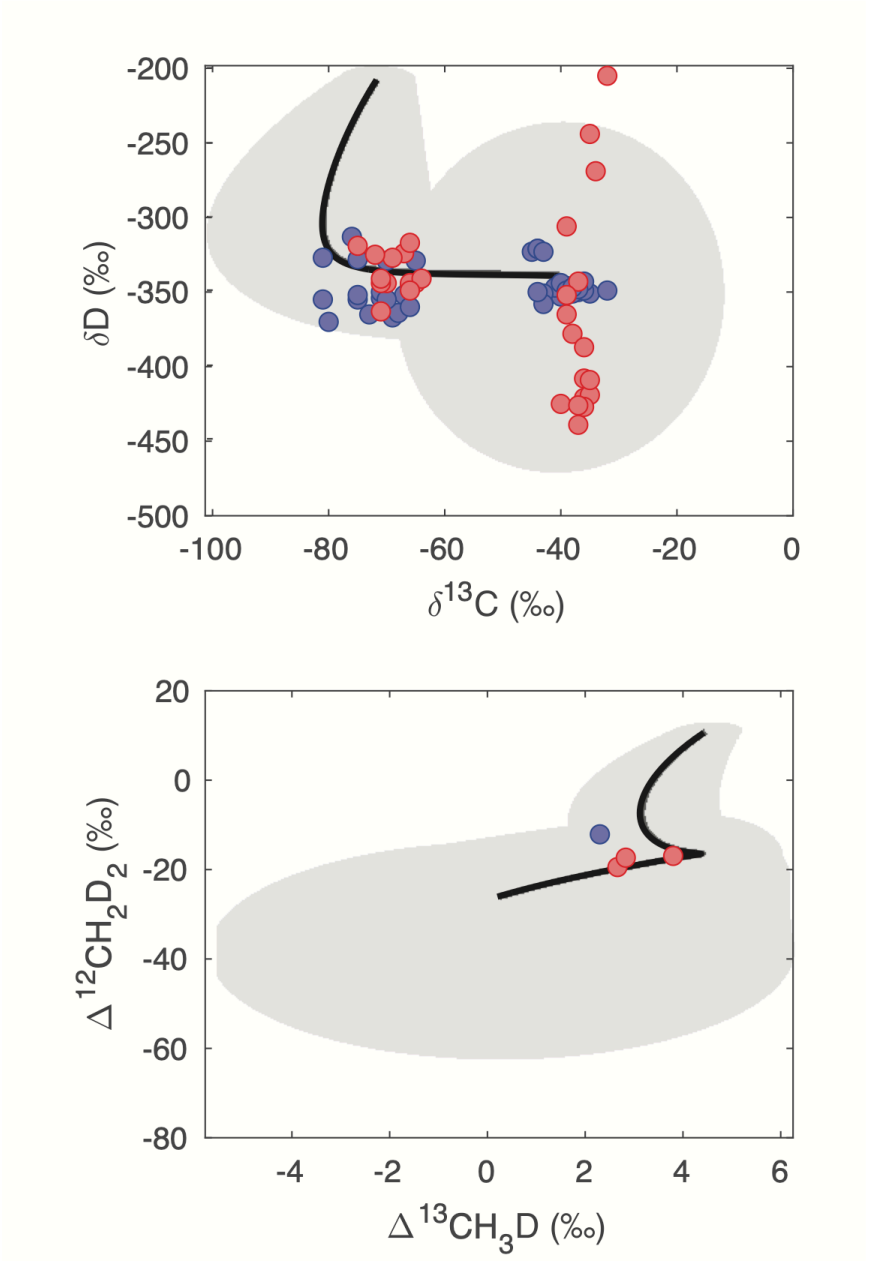

Figure 6: Results of isotopologue flow network model plotted in $\delta^{13}C$ versus δD (A) and $\Delta^{13}CH_3D$ versus $\Delta^{12}CH_2D_2$ (B), using the same model results as Figure 5. The grey area shows the results of Monte Calro simulation (n=1000) for 67% confidence interval calculated from covaricance matrix. Data from laboratory cultures are the same as those in Figure 5.

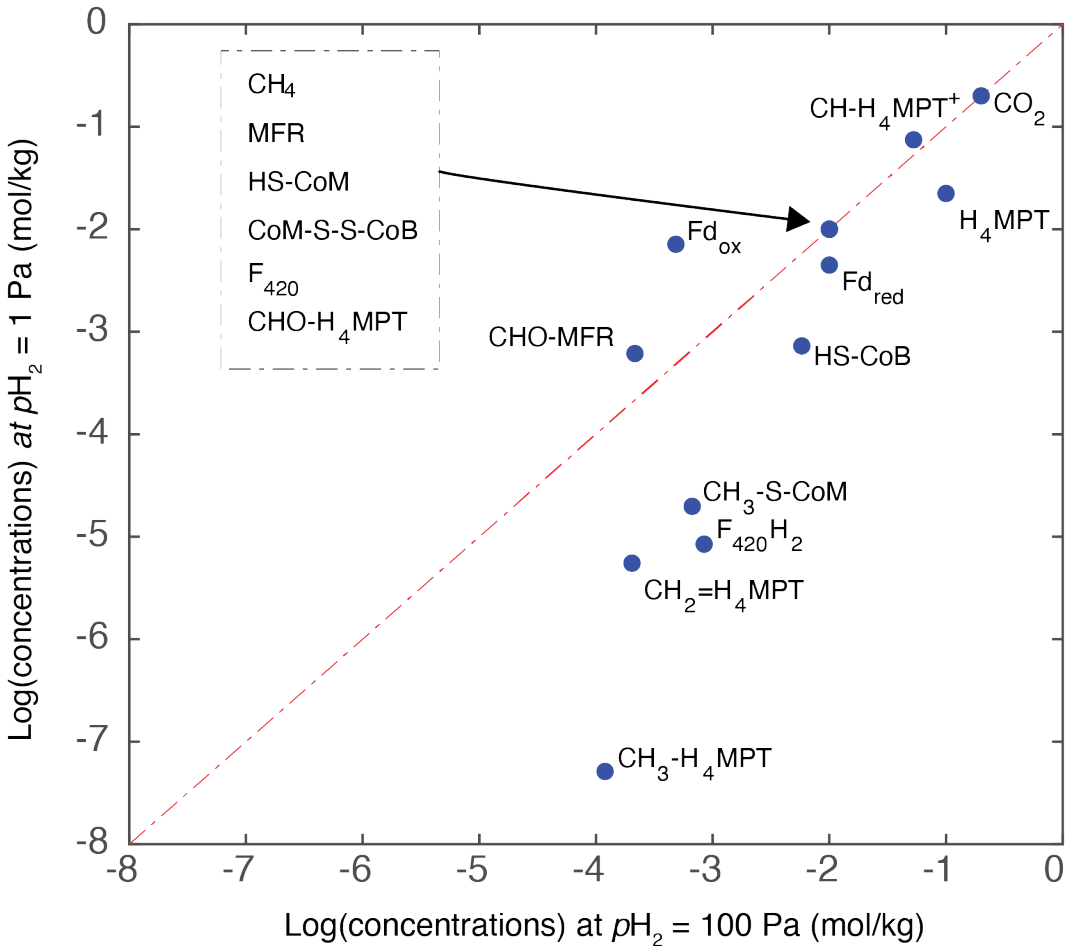

Figure 7: Results of the protein cost model for *in vivo* metabolite concentrations at pH_2 of 100 Pa and 1 Pa. Red line is the 1:1 line, and blue circles are the estimated metabolite and cofactor concentrations. Acronyms for chemical species are found in Table 1.

Tables

Table 1: The reactions for the pathway of hydrogenotrophic methanogenesis considered in the model. The standard free energy change of the reaction ($\Delta G^{0'}$) is for temperature at 25°C, H_2, CO_2, and CH_4 in the gaseous state at 1 bar, pH at 7, and dissolved compounds at 1 molar activity. The values for $\Delta G^{0'}$ were taken from Thauer et al (2008).

i	Reaction	$\Delta G^{0'}$ (kJ/mol)
1	CO_2 + MFR + Fd_{red} + $2H^+$ = CHO-MFR + Fd_{ox} + H_2O	0
2	CHO-MFR + H_4MPT = CHO-H_4MPT + MFR	-5
3	CHO-H_4MPT + H^+ = CH≡H_4MPT$^+$ + H2O	-5
4	CH≡H_4MPT$^+$ + $F_{420}H_2$ = CH_2=H_4MPT + F_{420} + H^+	6
5	CH_2=H_4MPT + $F_{420}H_2$ = CH_3-H_4MPT + F_{420}	-6
6	CH_3-H_4MPT + HS-CoM = CH_3-S-CoM + H_4MPT	-30
7	CH_3-S-CoM + HS-CoB = CH_4 + CoM-S-S-CoB	-30
8	H_2 + Fd_{ox} = Fd_{red} + $2H^+$	16
9	H_2 + F_{420} = $F_{420}H_2$	-11
10	$2H_2$ + CoM-S-S-CoB + Fd_{ox} = HS-CoM + HS-CoB + Fd_{red} + $2H^+$	-39

F_{420}: coenzyme F_{420}, Fd: ferredoxin, H_4MPT: tetrahydromethanopterin, CoB: coenzyme B, CoM: coenzyme M, MFR: methanofuran

Table 2: Notations and symbols used in this study

Symbols	Description and typical unit
Protein pathway model	
M_i	Molecular mass of enzyme that catalyzes the reaction *i* (kDa=kg/mol)
$k_{cat,i}$	Turnover number for enzyme that catalyze the reaction *i* (s^{-1})
$K_{m,kj}$	Half saturation constant for substrate *k* in reaction *i* (mol/kg)
$\Delta G_{r,i}$	Free energy of reaction *i* (kJ/mol)
J_{net}, J^+, J^-	Pathway flux (net, forward, and reverse) for reaction *i* (mol g-protein^{-1} s^{-1})
Λ	Cost function of PPM (g-protein sec mol^{-1})
N_{cell}/V	Cell density (cells/mL)
csMPR	Cell specific methane production rate (mol CH_4 cell^{-1} h^{-1})
k_La	Volumetric mass transfer coefficient (h^{-1})
K_H	Henry's law constant (mol kg^{-1} Pa^{-1})
pH$_2$	Partial pressure of hydrogen (Pa)
mH$_2$	Dissolved hydrogen concentration (mol/kg)
ϕ_i	Reversibility of reaction *i* ($\phi_i = J_i^-/J_i^+$)
Isotopologue flow network model	
r_j, d_j, q_j, u_j	Isotopologue ratios ($^{13}C/^{12}C$, D/H, $^{13}CD/^{12}CH$, and D_2/H_2) for substrate *j*
r_0, d_H	$^{13}C/^{12}C$ ratio of $CO_{2(g)}$ and D/H ratio of water
$(^x\sigma/\sigma)_j$	Symmetry ratios for ^{13}C and/or D isotopologues (*x=d, q or u*) relative to ^{12}C-H isotopologue for substrate *j*
α_i^+, α_i^-	$^{13}C/^{12}C$ KIE (forward and backward) for reaction *i*
α_{pi}^+, α_{pi}^-	Primary D/H KIE
α_{si}^+, α_{si}^-	Secondary D/H KIE
α_{cpi}^+, α_{cpi}^-	Primary KIE for clumped ^{13}C-D substrate for reaction *i* ($\alpha_{cpi}^+ = \gamma_{cpi}^+ \alpha_i \alpha_{pi}$)
α_{csi}^+, α_{csi}^-	Secondary KIE for clumped ^{13}C-D substrate for reaction *i* ($\alpha_{csi}^+ = \gamma_{csi}^+ \alpha_i \alpha_{si}$)
α_{dpi}^+, α_{dpi}^-	Primary KIE for clumped D_2 substrate for reaction *i* ($\alpha_{dpi}^+ = \gamma_{dpi}^+ \alpha_{pi} \alpha_{si}$)
α_{dsi}^+, α_{dsi}^-	Secondary KIE for D_2 substrate for reaction *i* ($\alpha_{dsi}^+ = \gamma_{dsi}^+ \alpha_{si}^2$)
γ_{xi}^+, γ_{xi}^-	Clumped KIE (*x=cp, cs, dp, ds*) for reaction *i*
α_{xi}^{eq}	Equilibrium fractionation factor (*x*=none, *p, s, cp, cs, dp, or ds*)

Table 3: Kinetic parameters for enzymes used in this study and their reference sources. Most enzymes were assayed at 37°C except for reactions-1, -3, and -5, which were assayed at 55 or 65 °C. The turnover rate (k_{cat}) for reaction-5 is corrected with reported activation energy of 34 kJ/mol. Reactions-1 and -3 are used without temperature corrections. Reactions-3 and -4 are only assayed in the reverse direction.

i	Enzyme	E.C. number	Mass (kDa)	k_{cat} (s^{-1})	K_{m1} (mM)	K_{m2} (mM)	*Note*	*Ref.*
1	CHO-MFR dehydrogenase	1.2.7.12	145	15	0.10		K_{m1} for MFR	1
2	CHO-MFR:H_4MPT formyltransferase	2.3.1.101	35	2158	0.4	0.4	K_{m1} for COH-MFR, K_{m2} for H_4MPT	2
3	CH≡H_4MPT$^+$ cyclohydrolase	3.5.4.27	42	1400	0.1		K_{m1} for CHO-H_4MPT	3
4	CH_2=H_4MPT dehydrogenase	1.5.98.1	35	320	0.006	0.018	K_{m1} for CH_2=H_4MPT, K_{m2} for F_{420}	4
5	CH_2=H_4MPT reductase	1.5.98.2	36	641	0.015	0.012	K_{m1} for CH_2=H_4MPT, K_{m2} for $F_{420}H_2$	5
6	CH_3-H_4MPT: CoM methyltransferase	2.1.1.86	380	65	0.135	0.277	K_{m1} of CH_3-H_4MPT and K_{m2} for HS-CoM	6
7	CH_3-CoM reductase	2.8.4.1	270	31	0.17	0.17	K_{m1} for CH_3-S-CoM, K_{m2} for CoB	7,8
10	H_2:CoB-CoM heterodisulfide, ferredoxin reductase	1.8.98.5	229	76	0.5	0.015	K_{m1} for CoM-S-S-CoB, Km_2 for Fd_{oxi}	9

reference: 1, Bertram and Thauer (1994), 2:Beritung and Thauer (1990), 3: Beritung et al.(1991), 4:Brommelstroet et al. (1990), 5:Ma and Thauer (1990), 6: Lienard et al. (1996), 7: Wongate and Ragsdale 2015, 8: Dey et al.(2010), 9: Kaster et al. (2011).

Table 4: Isotopologue ratios for carbon ($\delta^{13}C$), hydrogen (δD), $\Delta^{13}CD$ and ΔD_2 values expected for equilibrium at 25°C based on equilibrium fractionation factors from Gropp et al. (2020) and Horita and Wesolowski (1994). Carbon and hydrogen isotope fractionation factors are referenced against gaseous CO_2 and liquid water, respectively.

j	Species	$\delta^{13}C$	δD	$\Delta^{13}CD$	ΔDD
1	$CO_{2(g)}$	0.00	*n.a.*	*n.a.*	*n.a.*
2	CHO-MFR	-17.57	-142.20	4.48	*n.a.*
3	CHO-H_4MPT	-19.23	-149.40	4.21	*n.a.*
4	CH≡H_4MPT$^+$	-15.95	-87.16	4.56	*n.a.*
5	CH_2=H_4MPT	-32.66	-12.85	4.76	13.37
6	CH_3-H_4MPT	-47.67	-92.61	5.22	15.61
7	CH_3-S-CoM	-64.61	-130.82	5.49	15.61
8	CH_4	-66.34	-177.82	5.74	18.50
	$H_2O_{(v)}$	*n.a.*	-73.00	*n.a.*	*n.a.*
	$H_2O_{(l)}$	*n.a.*	0.00	*n.a.*	*n.a.*

n.a., not applicable.

Table 5: Isotopologue reactions considered for the last step of methanogenesis (reaction-7).

Reaction	Forward KIE	Reverse KIE
$^{12}CH_3$-R + H ↔ $^{12}CH_4$ + R	1	1
$^{13}CH_3$-R + H ↔ $^{13}CH_4$ + R	α_{7}^{+}	α_{7}^{-}
$^{12}CH_3$-R + D ↔ $^{12}CH_3D$ + R	α_{p7}^{+}	¼ α_{p7}^{-}
$^{12}CH_2D$-R + H ↔ $^{12}CH_3D$ + R	α_{s7}^{+}	¾ α_{s7}^{-}
$^{13}CH_3$-R + D ↔ $^{13}CH_3D$ + R	$\alpha_{cp7}^{+} = \gamma_{cp7}^{+}\alpha_{7}^{+}\alpha_{p7}^{+}$	¼ α_{cp7}^{-} = ¼ $\gamma_{cp7}^{-}\alpha_{7}^{-}\alpha_{p7}^{-}$
$^{13}CH_2D$-R + H ↔ $^{13}CH_3D$ + R	$\alpha_{cs7}^{+} = \gamma_{cp7}^{+}\alpha_{7}^{+}\alpha_{s7}^{+}$	¾ α_{cs}^{-} =¾ $\gamma_{cp7}^{-}\alpha_{7}^{-}\alpha_{s7}^{-}$
$^{12}CH_2D$-R + D ↔ $^{12}CH_2D_2$ + R	$\alpha_{dp7}^{+} = \gamma_{dp7}^{+}\alpha_{p7}^{+}\alpha_{s7}^{+}$	½ α_{dp7}^{-} = ½ $\gamma_{dp7}^{-}\alpha_{p7}^{-}\alpha_{s7}^{-}$
$^{12}CHD_2$-R + D ↔ $^{12}CH_2D_2$ + R	$\alpha_{dp7}^{+} = \gamma_{ds7}^{+}(\alpha_{s7}^{+})^2$	½ α_{dp7}^{-} = ½ $\gamma_{ds7}^{-}(\alpha_{s7}^{-})^2$

Table 6: $^{13}C/^{12}C$ and D/H KIE values used in this study. *See* Table 2 for description of the notation. Values shown in italic letters are prescribed fractionation factors (and 1σ values). Values shown in non-italic letters are derived values using equation-18 and -19.

Reactions	α^+	α^-	α_{ip}^+	α_{ip}^-	α_{is}^+	α_{is}^-
1	*0.960±0.02*	0.9772	0.703	*0.82±0.20*	*n.a.*	*n.a.*
2	*0.960±0.02*	0.9616	*n.a.*	*n.a.*	*0.85±0.05*	0.857
3	*0.960±0.02*	0.9568	*n.a.*	*n.a.*	*0.85±0.05*	0.792
4	*0.960±0.02*	0.9766	0.810	*0.82±0.20*	*0.85±0.05*	0.786
5	*0.960±0.02*	0.9751	0.744	*0.82±0.20*	*0.85±0.05*	0.925
6	*0.960±0.02*	0.9774	*n.a.*	*n.a.*	*0.85±0.05*	0.887
7	*0.960±0.01*	0.9618	0.337	*0.41±0.04*	*0.85±0.01*	0.899

n.a., not applicable.

Table 7: Clumped KIE values used in this study. *See* Table 2 for a description of the notation. Values shown in italic letters are prescribed fractionation factors (and 1σ values). Values shown in non-italic letters are derived values using equation-20.

Reactions	γ_{cp}^+	γ_{cp}^-	γ_{cs}^+	γ_{cs}^-	γ_{dp}^+	γ_{dp}^-	γ_{ds}^+	γ_{ds}^-
1	*1.000±0.008*	0.9955	*n.a.*	*n.a.*	*n.a.*	*n.a.*	*n.a.*	*n.a.*
2	*1.000±0.008*	0.9958	*1.0000*	1.0003	*n.a.*	*n.a.*	*n.a.*	*n.a.*
3	*1.000±0.008*	0.9955	*1.0000*	0.9997	*n.a.*	*n.a.*	*n.a.*	*n.a.*
4	*1.000±0.008*	0.9953	*1.0000*	0.9998	*1.000±0.010*	0.9868	*n.a.*	*n.a.*
5	*1.000±0.008*	0.9948	*1.0000*	0.9995	*1.000±0.010*	0.9846	*1.0000*	0.9978
6	*1.000±0.008*	0.9945	*1.0000*	0.9997	*1.000±0.010*	0.9846	*1.0000*	1.0000
7	*1.000±0.008*	0.9943	*1.0000*	0.9998	*1.000±0.010*	0.9818	*1.0000*	0.9972

n.a., not applicable.